UNIVERSIDAD CARLOS III DE MADRID

‘Study of micro-illumination techniques with optical fibers and its application in diagnostic methods’

Bachelor Thesis

Dept. of Bioengineering and Aerospace Engineering

September 2014

Universidad Carlos III de Madrid

Autor: Cristina Herráez Muñoz
Tutor: Jorge Ripoll
Director: Jose Luis Muñíz Gutiérrez

Acknowledgements

Muchas son las personas que han hecho posible que este momento haya llegado.

En primer lugar dar gracias a Dios. Gracias por darme tanto, por darme todo.

A mi familia. Gracias por no dudar de mí en ningún momento y por saber ponerme los pies en la tierra cuando ha sido necesario. Papá y mamá, gracias por mostrarme vuestro amor de una forma en la que muy pocas personas son tan buen ejemplo, en forma de sacrificio. Gracias por ver mis oportunidades como vuestras propias. Gracias Bea, Borja y Oriol, espero poder aportaros algún día todo lo que me aportáis vosotros a mí. A mis abuelas, por inspirarme.

A Jorge Ripoll y Jose Luis Muñíz, por vuestro apoyo y atención durante estos meses.

Mil gracias Pedro, por tu infinita paciencia. Por enseñarme, aconsejarme y por dedicarme tu tiempo. He aprendido mucho de ti, muchas gracias de corazón.

Gracias Lucía, Laura, María, Nuria, Alicia, Aida, Lidia, Isa… los mejores momentos en estos 4 años llevan vuestro nombre. Gracias por vuestra sincera amistad.

A Edu, por tu apoyo. Gracias Marcos, gracias.

Finalmente gracias a los que me apoyaron en la decisión de volver a Viena. Con vuestras sonrisas, vuestras palabras de ánimo, con vuestros mejores deseos hacia mí sabiendo que el camino no sería fácil pero que apoyo no me iba a faltar.

Index

List of Acronyms

CT = Computer tomography

DTF = Detector transfer function

IR = Infrared

LED = Light-emitting diode

MRI = Magnetic resonance imaging

MSE = Mean squared error

NA = Numerical aperture

NIR zone = Near-infrared zone

PIN photodiode = Positive intrinsic negative photodiode

POF =Polymer optical fiber

RBC = Red Blood Cells

Introduction

Optical imaging techniques and spectroscopy constitute emerging alternatives to other imaging modalities in which electromagnetic radiation or nuclear energy is used for the study of biological tissues [1]. This is due to the fact that properties of a tissue in optical terms (i.e. light penetration and energy deposition via absorption) are closely related to diagnostic as well as therapeutic procedures [2]. Promising optical techniques have been developed over the past three decades since they provide great advantages making them particularly interesting for clinical environment overcoming results obtained by using other kind of light sources. The response obtained out of an optical system could be an electrical response or an acoustic response, among others, used in NIR spectroscopy, photoacoustics and optogenetics techniques [3].

Advantages over other modalities include the use of non-ionizing radiation (i.e it does not use any radioactive component). Non-ionizing radiation does not produce a health issue even when exposure to it is long. Consequently, this opens the possibility to obtain repeatable, quantitative and calibrated data out of its use. The scope has evolved from highly controlled to a manageable clinic use [4]. Another advantage is that, measurements obtained out of an optical system are linked to changes in molecules (hemoglobin, lipids, water…) that may be associated with diseases, such as cancer [5]. Ability to properly interpret these changes might lead to the differentiation between normal and diseased tissue so that early diagnosis and treatment is possible. The sensitivity of the technique, its relative inexpensiveness and its use in the study of a biological tissue *in vivo* makes it interesting in applications regarding functional brain mapping and breast cancer diagnosis [5, 6, 7]. Is important to notice that optical techniques can be used independently or combined with optical biopsy techniques (e.g tissue autofluorescence) or with techniques as MRI or CT, for example.

The use of this technology allows the use of intense sources of light (laser, diodes…) which are small and reliable. Linked to those sources of light, optic fibers allow conducting the light to localized parts of the body, so the response to the illumination is localized. Penetration depth of light is small compared to the penetration of ultrasound, for example [8, 9]. However, depth highly varies until reaching the centimeter scale by choosing the right wavelengths and using the right emitter-detector distance. Wavelengths that allows imaging at several centimeters deep in tissue are in the near-infrared, so that the optical range is found at 600-1000nm [11].

Visible light and near-infrared (NIR) light interact with tissues mainly through absorption and scattering [12]. Out of this interaction, information about structure and specific features can be used to distinguish between pathologies [13].

Lasers, diodes and optical fibers are crucial for the development of these techniques. For that and in this concrete work, we will characterize the illumination of an optical fiber (emitter and detector). Optical fibers are considered as light transmitter. However, they are not just transmitters but they perturb the input light in a specific way. Optical fibers locally illuminate a specific part of the body but not in a completely innocuous way so that transmission of light is modulated.

Calculation of the extinction (sum of the absorption and scattering) is done by solving the inverse problem needed for the characterization of turbid biological tissues. Most of the information will be contained in the absorption coefficient, μ_a, and in the scattering coefficient μ_s meaning that, at large distances, light diffusion is dominant [14].

Here, we will study not only the illumination in opaque surfaces but in turbid tissues where light is transmitted into the tissue. The direction of the ray transmitted will completely determine the response of our system. In order to characterize the optical fiber, a model should be developed that takes into account not only the illumination pattern but also the direction of that illumination, following Figure 1.1.

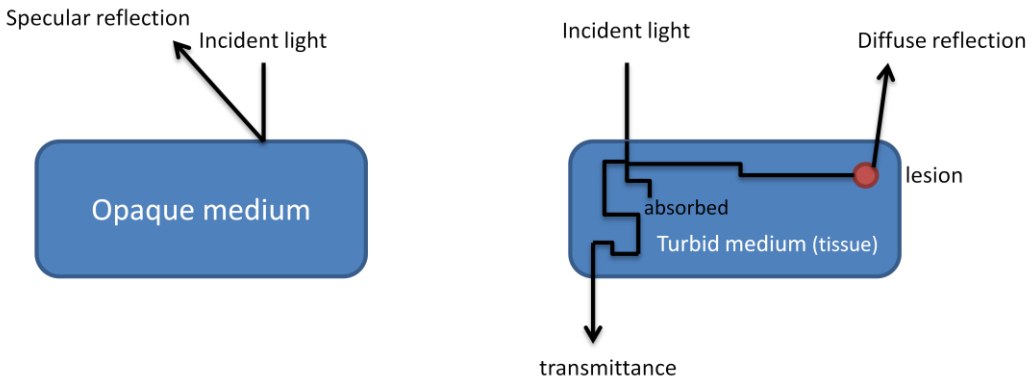

Figure 1.1 Illumination in an opaque medium (left) and in a turbid medium (right),

Concretely, the use of big optical fibers such as polymer optical fibers (POF) with 1 mm of diameter allows easy handling since they are easy to prepare and model [15]. The study can be extended to the use of other commercially available optical fibers, including monomode fibers of 9µm of diameter.

The scope of the project is to characterize the illumination in our specific system, although possibilities extend to be able to measure any effect that light produces (optical, acoustic or electric effect) not only used to illuminate but also to excite (increasing the chances not only to diagnosis but also to the therapy, as previously mentioned).

The working place provided for the development of the project was perfectly suitable in order to overcome the physical part of the analysis. Since the first objective for the development of the measuring system was not the analysis of biological tissues and emulsions but the analysis of metallic (opaque) surfaces, the laboratory was not prepared for biological studies and sample preparations. Due to the lack of time and the difficulties to maintain the samples in a good state, selected tissues and turbid media were simple, easy to handle, prepare and maintain. For this first phase of the study, characterization was done in a controlled media. As a next stage this would be applied to more complex tissues.

Materials and Methods

Fiber Preparation

Optical fibers used in the analysis were prepared in the lab by using the appropriate tools. After cutting the fibers with the desire length, different sandpapers were used. The scenario is presented in Figure 2.1.

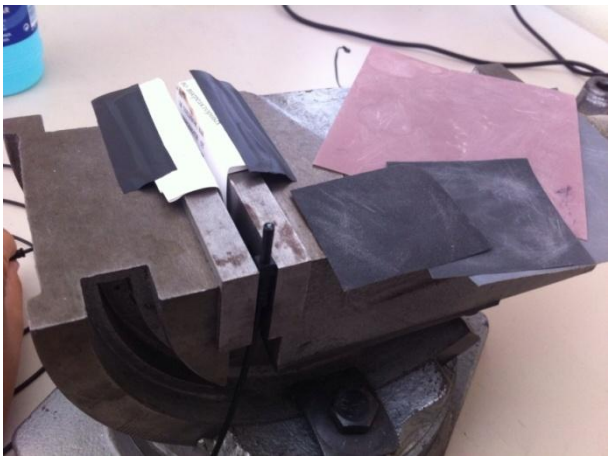

Figure 2.1 Preparation of fibers.

In the figure three different sandpapers can be seen; the biggest of 800 grit for processing. In order to obtain a surface as smooth as possible, a file for polishing was used after the sandpapers. Following the polishing step, ethanol was used to eliminate any small particles to complete the preparation. Different lenses were used to ensure a correct procedure during fiber filing.

Biological samples (portions of meat) were used to analyze their optical properties and were taken from different animals. Slices were obtained from bigger pieces by using a cutter. The procedure allowed obtaining smooth surfaces in case they were needed or selection of proper zones of interest without the need of large equipment.

Methods

The measuring system (Fig. 2.2) used, developed at CIEMAT, is based on a scanner and a fiber-coupled detector attached to it, able to move along the three Cartesian axis (X,Y,Z) by means of stepper motors. One step in the X-Y plane corresponds to 4 μm, while one step in the Z axis implies a displacement as small as 1.25 μm.

To save time only scans in the Y-Z plane have been done in the most part of this work, approximation that leads to reasonable results taking into account the cylindrical symmetry of the optical fibers.

The fiber-coupled detector consists of a PIN photodiode [16] directly attached (butt-coupled [17]) to a polymer optical fiber (POF). These are cheap and easy to use multimode fibers mainly used for local area communications [18]. The (receiver) fiber used in the study is 50 cm long and has a diameter of 1 mm (0.9 of core diameter) permitting, in the ideal case, the propagation of more than 10^6 modes [19].

Due to the fact that the wavelengths employed (400-1000 nm) are much lower than the involved sizes, the "Geometrical Optics" theory applies and thus the light propagation will be represented as "rays" along the entire work [20].

The detector movement (scanning) is controlled by a PC through the parallel port which sends the electric signals to the motors changing their positions one step. Light detected by the photodiode is amplified and digitized with 16 bits of resolution and the data are read by the PC for each position of the sensing head. The PC also controls the light sources (LEDs) though a programmable current source.

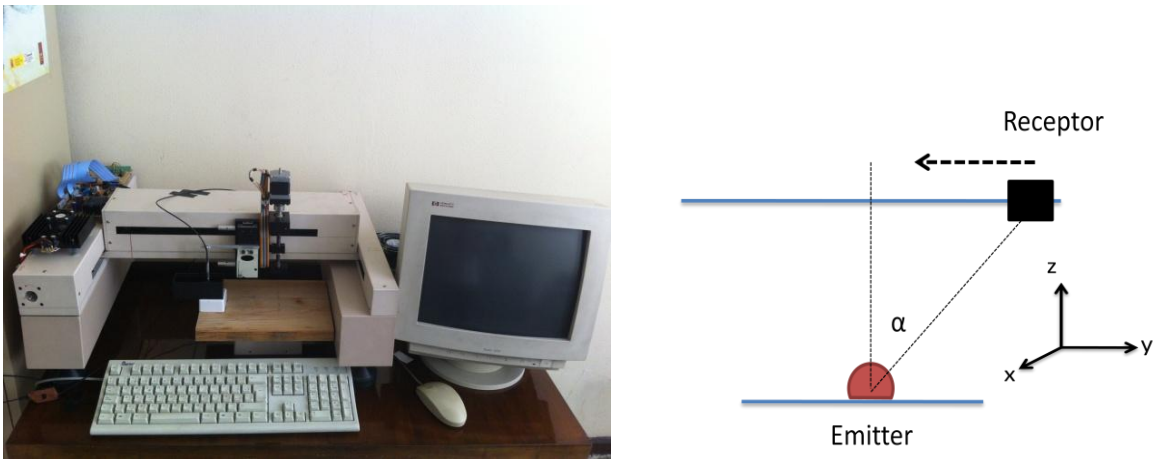

Figure 2.2. Photograph and schematic drawing of the measuring system.

Results

Characterization of the measuring system in transparent media

3.1. Introduction

In order to assure an accurate determination of the illumination patterns on actual samples, an initial step consisting of a fine characterization of the system used to perform these measurements is needed. To do this, the response of the measuring system to the light emitted by well known sources propagating in transparent media will be studied. These media have been chosen because their lack of appreciable absorption and scattering guarantees straight paths and energy conservation. Examples of transparent media that fulfill these properties at short-range are air and pure water [21].

The final result sought is to "calibrate our meter", i.e. to find the system transfer function that allows us to solve the inverse problem of finding the true spatial distribution of the energy transferred to the medium. In our case, this transfer function refers to the directional detection response of the system.

3.2. Characterization of the detector

As mentioned before, the detector will be characterized using a known light point source, a white LED with large viewing angle [22] (greater than the nominal numerical aperture [23] of this optical fiber, 0.5). Fig. 3.1a shows the radiation pattern – emission intensity vs. the angle between the ray and the normal – from the datasheets. The usual model for this kind of emission is a generalized Lambertian [24], as the given in the onset of figure 3.1.b. This figure shows some of these patterns, from a pure Lambertian one (m=1) to a high directional emission (m=70), together with the one most similar to the manufacturer's curve (m=0.5), approximation quite suitable up to 75°.

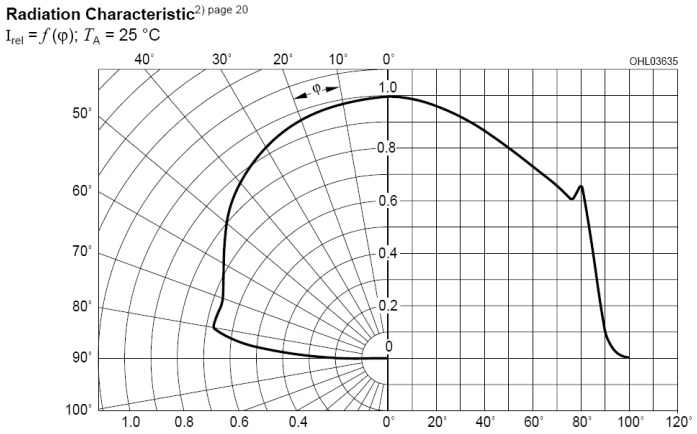

(a)

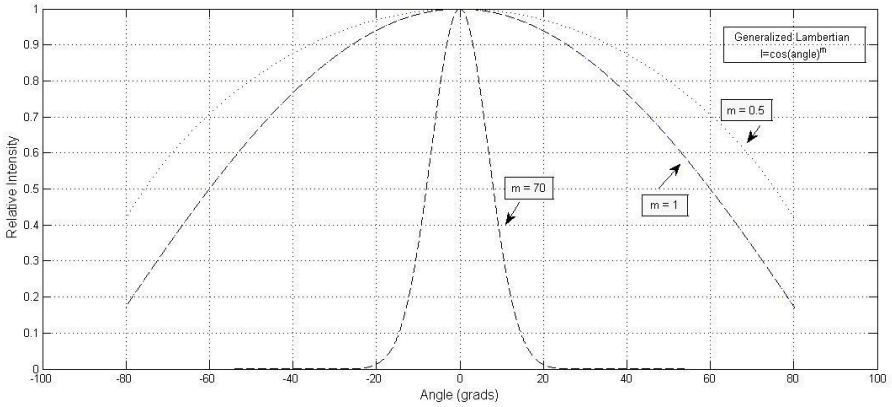

(b)

Figure 3.1. Source radiation characteristics (a): from the datasheets; (b) from the model.

3.3. Theoretical foundations

The starting point is the *Cosine and Inverse Squared Law* [25], that states that the energy received by an elemental area, *dS*, due to a bundle of rays emitted from a point source with intensity *I*, located at a distance r from the area and forming an angle θ with its normal (figure 3.2) is:

$$E = I \cdot \frac{cos\theta}{r^2} \qquad \text{[Eq. 3.1]}$$

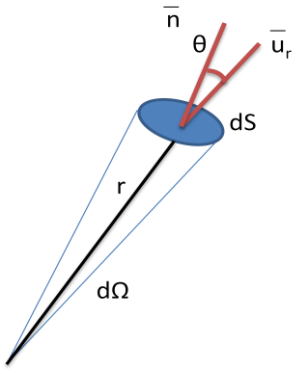

Figure 3.2. Geometry of the illuminance.

In our case, the point source is the LED and the detection area is the entrance part of the receiver fiber (1 mm of diameter). For distances *r* greater than some orders of magnitude this diameter, the entire fiber's surface can be considered as the elemental area *dS*. For shorter distances, an extended receptor should be formed by integrating the contributions of each *dS*.

Since the LED contains a lens, the determination of the exact position of the point emitter is not possible if one only measures distances. In order to determine the exact position, we make use of the following relation directly derived from the *Cosine Inverse Law* that expresses the fact that the energy E detected by the *same* detector multiplied by the squared distance is constant (figure 3.3):

$$\mathrm{E}_1 \cdot {d_1}^2 = \mathrm{E}_2 {d_2}^2 \qquad \text{[Eq. 3.2]}$$

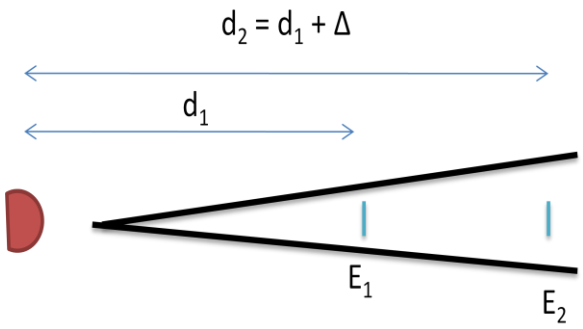

Figure 3.3. Determination of the exact point source position.

The detection fiber, after performing a measurement, is moved along the Z axis (coincident with the LED's optical axis) a precise increment Δ and another measurement is taken. Applying equation 3.2 the initial position, d_1, of the emitter can be found with great accuracy. Assuming that the exact position of the source is already known, the equations governing the emission-detection process are readily derived from basic 3D geometry.

If the point emitter is located in the XY plane at position (x_e,y_e,0) and the scanning is performed along the line (0,0,z=h_0) (figure 3.4), the following equations are fulfilled:

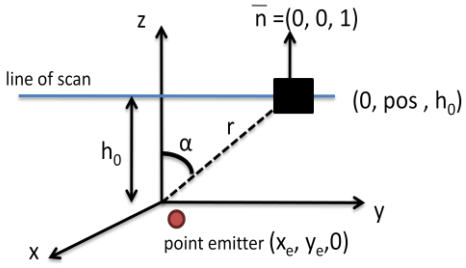

Figure 3.4. Geometry of the emission and detection of a light ray.

$$TE = r = (-x_e, pos - y_e, h_0)$$

$$|r| = \sqrt{{x_e}^2 + (pos - y_e)^2 + {h_0}^2}$$

$$n \cdot r = |n| \cdot |r| \cdot cos\alpha \qquad \text{[Eq. 3.3]}$$

$$cos\alpha = \frac{h_0}{\sqrt{{x_e}^2 + (pos - y_e)^2 + {h_0}^2}}$$

3.4. Initial measurements

In figure 3.5 a typical output from the scanning is displayed for $h = 27$ mm (distance that has been computed making use of Eq. 3.2.). The pattern has a bell like shape reaching its maximum when the source and the detection fiber are aligned (null angle). Another feature that can be seen is that the pattern is asymmetric, the leading edge being smoother than the trailing one, thus indicating some small defect in the fiber-photodiode coupling.

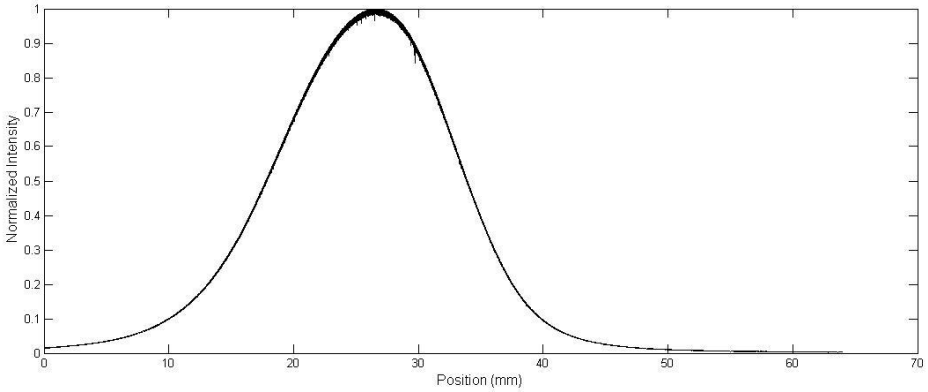

Figure 3.5. Typical output obtained from the detector

An increment in the distance of the system is readily translated in a decrease in the intensity, as shown in Fig. 3.6.

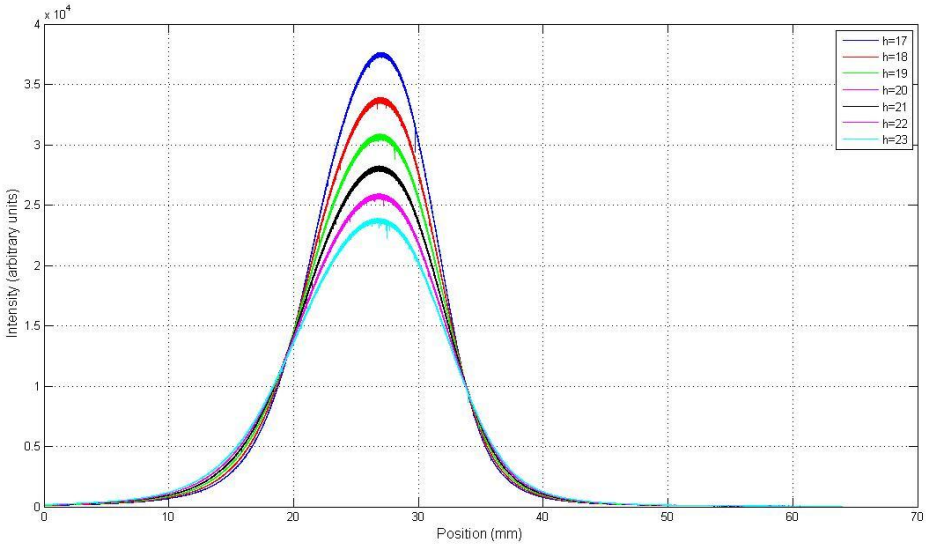

Figure 3.6. Intensities obtained from scannings at several distances source - fiber tip.

3.5. Analysis of data

3.5.1 Air

The angular response (detector transfer function, DTF) of the fiber-coupled-detector can be approximated to a super-Gaussian function [26] of low index (n=2.5):

$$DTF = e^{(-2.\frac{|\alpha|}{w})^n} \qquad \text{[Eq 3.4]}$$

where α is the angle of the ray with the normal surface and w is related to the width of the function and should be experimentally adjusted. To take into account the aforementioned asymmetry of the curves, the parameter w is actually divided in two: one, w_1, for negative angles and other slightly different, w_2, for positive angles. They are adjusted by the usual procedure of minimizing the mean squared error [27], finding the following optimum values:

$$w_1 = 0.51 \qquad\qquad w_2 = 0.44$$

both differing in 14%, values compatible with the nominal numerical aperture. With these parameters, it is possible to fit the experimental data to a theoretical model that, in each position of the scan, performs the product of the three contributions:

$$Output\ (position) = DTF(air) * Geometry\left(\frac{cos\alpha}{h^2}\right) * IntensityLED(cos^{0.5}\alpha) \qquad \text{[Eq 3.5]}$$

Resulting in an excellent fit, as shown in figure 3.7 where both normalized experimental and fitted patterns have been plotted together for a distance source-fiber large enough (30 mm) to consider this last one as a elemental area. The coefficient R^2 [28] equals to 0.998.

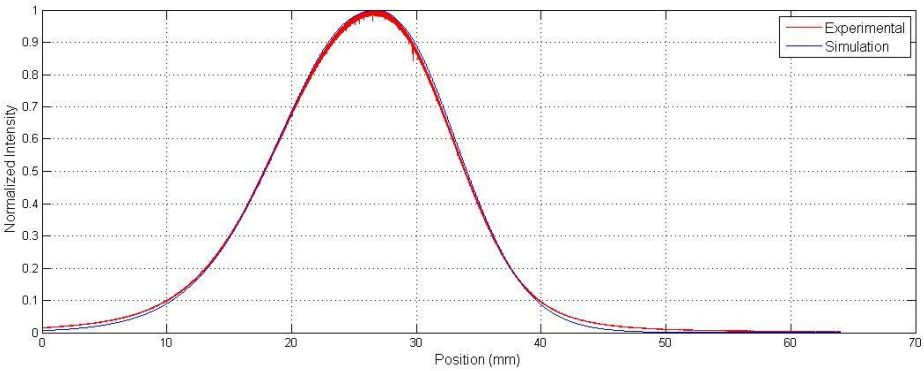

Figure 3.7. Experimental and fitted output scanning curves in air.

3.5.2. Water

The emission diagram of the LED given in the datasheets is in air (see Fig 3.1), but the pattern must be different when it is immersed in pure water (and electrically sealed). In order to find the new emission diagram, the *Snell Law of Refraction* [29] is applied assuming an interface of air between the LED's lens and the water (Fig 3.8).

Under this assumption, each ray emitted by the source following the nominal emission diagram in air is converted into a new ray for water.

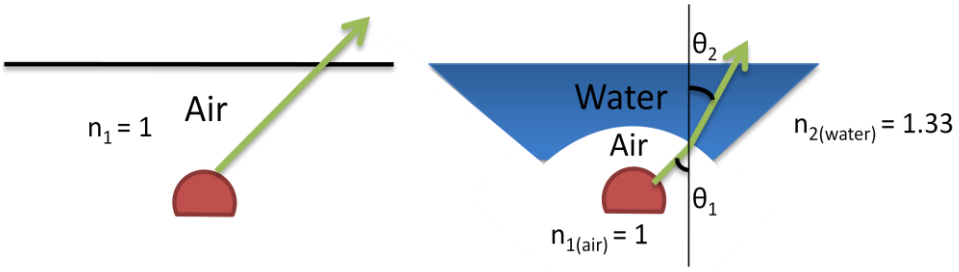

Figure 3.8. Approximation used to find the LED emission diagram in water.

$$n_1 \cdot \sin\theta_1 = n_2 \cdot \sin\theta_2$$

From the refraction law,

$$\theta_1 = \sin^{-1} 1.33 \cdot \sin\theta_2 \qquad \text{[Eq. 3.6]}$$

Equation 3.6 allows to determine the normalized radiation diagram. This should be corrected by a factor (in our case, 1.57) that assures that the LED emission is the same in both cases (in air and in water) as shown in Figure 3.9. In other words, both curves must have the same area, although the estimated pattern in water is narrower and higher at the peak. These facts justify the experimental finding that the output obtained for the same distance and the same LED current greatly differs in air and in water (see figure 3.10). In effect, while both total emissions are the same, the quantity of light than effectively enters the receiver fiber is greater because more light is emitted at the apex.

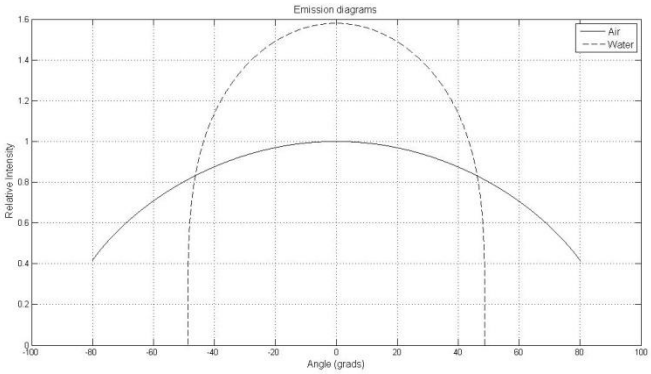

Figure 3.9. Comparison between the emission diagram in air and the estimated one in water.

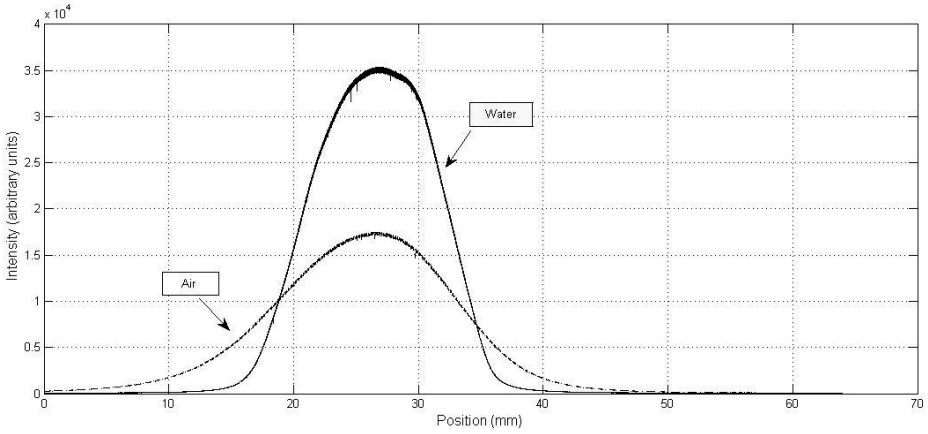

Figure 3.10. Comparison betwen air and water response in the same conditions.

This concentration of rays in the central part highlights that the emision in water medium is different, leading to different optical responses. This response has been estimated in a way similar to the air case, assuming again a fiber's angular dependence of the type super-Gaussian (Eq. 3.4), now with an index $n = 3$. A MSE fitting lead to the following values of the corresponding widths for negative and positive angles:

$$w_1 = 0.35 \qquad\qquad w_2 = 0.33$$

This time both values are quite similar and coincident to a certain extent with the reduction of the numerical aperture corresponding to the difference in refraction indexes. The simulation of the response of the detector to the scanning, according to Eq. 3.7, together with the experimental result are displayed in Fig 3.11 with a confidence level of 0.996.

$$Output\ (position) = DTF(water) * Geometry\left(\frac{cos\alpha}{h^2}\right) * IntensityLED(cos^{0.5}\alpha_1) \text{ [Eq. 3.7]}$$

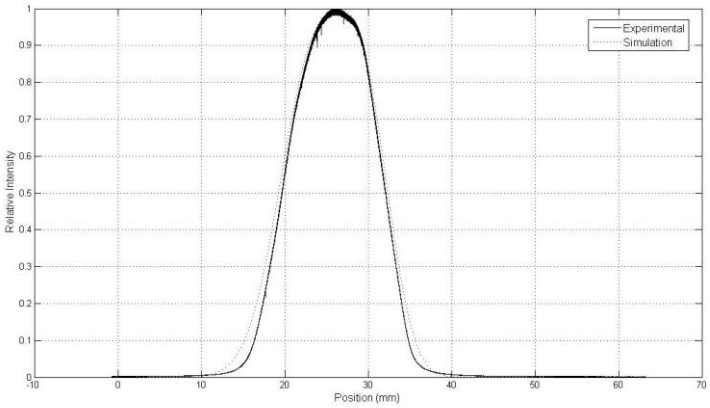

Figure 3.11. Experimental and fitted output scanning curves in water.

3.6 Near-field measurements

The analysis during this chapter has been done with the (point) source far away from the detector (the fiber tip), in conditions well falling within the far-field zone (distances around $h \approx 20mm$) [30]. However the characterization of the detector in the vicinity of the source (near-field) is needed as well. This cannot be done simply by putting both devices close because the LED behaves like a point source only for distances not too short. Moreover most of the LEDs have inner wires connecting the semiconductor with the leads that are "seen" as shadows when looking at it too close.

These shortcomings can be avoided if an emitter that resembles a true point source is used. A narrow single mode fiber, 9 µm of diameter, placed close (less than 1 mm) the receiver fiber tip will fulfill these requirements. A single mode fiber, allowing the propagation of only the fundamental mode, has a pure Gaussian emission pattern with a geometrical aperture of the order of 0.12 [31]. Thus the scanning of such a source yields an accurate characterization of the receiver at near-field.

Figure 3.12 shows a two dimensional (X-Y) scanning of the single mode fiber viewed with our detector placed at Z=0.5 mm in air. Since the illumination beam is so narrow, the light spot thrown on the fiber's surface is quite small (less than 0.1 mm) and so what we are seeing here are the inhomogeneities and defects of this fiber. The lack of round shape and some dark regions on the surface are noticeable features.

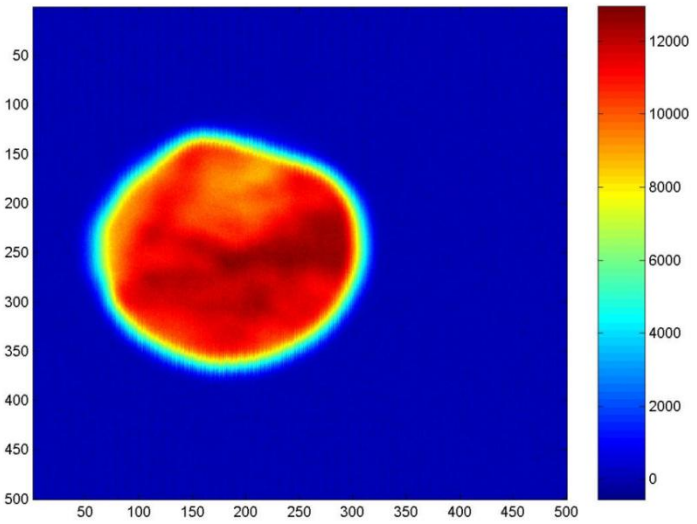

Figure 3.12. Color 2-D intensity plot of the single mode illuminating fiber.

A one-dimensional slice of this pattern is plotted in figure 3.13 (blue trace), where a defect at the left of the optical axis is seen. This reduction of intensity is due to a region on the surface that blocks some of the incident light, effect that disappears when the emitter fiber goes away from the receiver (red trace). In this last case, border between near and far fields, only the narrow Gaussian illumination from the single mode fiber remains.

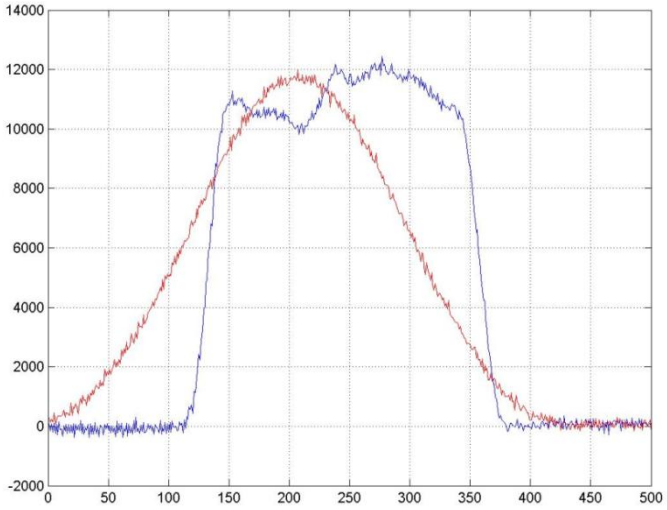

Figure 3.13. Intensity slices of the single mode fiber patterns at two distances.

This one-dimensional behavior can be accurately modeled by assuming that each point on the receiver tip surface is an elemental detector having an angular dependence equal to the far-field global response (found before) with a zone having a masking factor of 90 per cent in this case. Figure 3.14 shows this simulation that, taking into account all the simplifications made, fits quite well the real data (blue curve in figure 3.13).

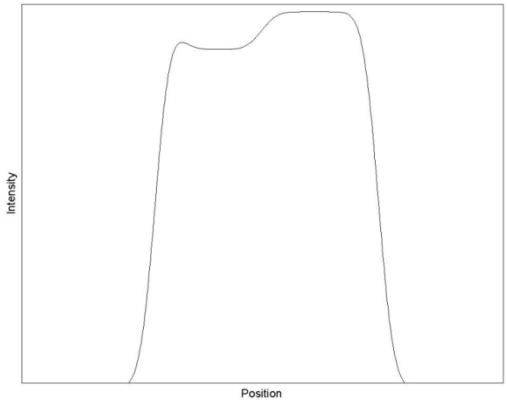

Figure 3.14. Simulation of the near field (0.5 mm) single mode illumination pattern.

3.7. Discussion

The optical fiber that operates as detector behaves like a super-Gaussian function of index slightly greater than 2 (2.5-3). The fact that is not exactly 2 (Gaussian function) and its asymmetry could be due to effects derived from the butt-coupling between fiber and detector. Optical fiber (1 mm of diameter) and photodetector have similar areas, which makes the procedure difficult to precise. In any case, the transfer functions have been successfully found and they have proven their suitability in many tests performed with LEDs of different wavelengths and remission characteristics.

Moreover, the numerical aperture (NA) of the fiber is compatible with the nominal value and lowers form air to water in a factor quite similar to the relation of refractive indexes (1.33). Finally, once the measuring system is characterized for air and water, it can be already extrapolated for other media and used to study the illumination produced by other fibers.

As a final and important remark, it should be mentioned that a large area fiber behaves at near field as an ensemble of elemental sensors all having the same directional characteristics, equal to the far-field angular global dependence. Defects present on the fiber surface must be taken into account in this case because they produce distortions in the illumination patterns, although at long distance they simply imply a reduction in the total amount of light with no appreciable effect on the shape of the light spot.

4.1. Introduction

Optical fibers are prepared and coupled to the light sources in different ways. These two facts make very difficult (if not impossible) to 'a priori' determine exactly which modes will be excited or which output intensity the system will have (a crucial factor for many applications, such as for instance the optical therapy [32]).

Excitation of modes depends on the source of light used. If this source is a LED, the fiber will be *overfilled* (this is, the source will theoretically excite all modes). If the source is a laser, the optical fiber will be *underfilled* (this is, only few modes will be excited), as shown in figure 3.1. However, even using a LED (as has been the case), not all the modes are excited since there is also an angular dependence. If the angle is not the optimal one, some modes won't be excited.

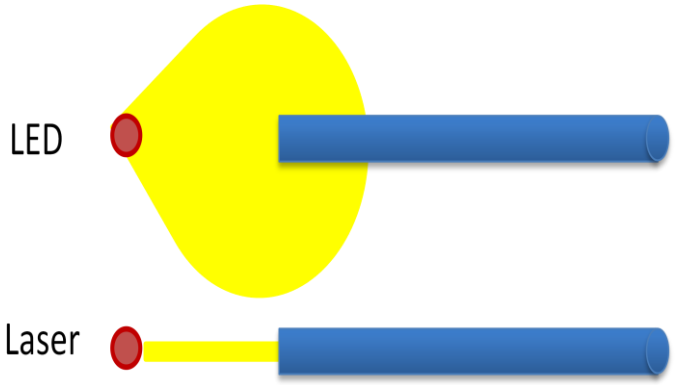

Figure 4.1. Sketch of the excitation of the fiber.

In our experiments *butt-coupling* between fiber and LED has been done, without additional optical elements in between. Even in this so simple case, different LEDs and different orientations of both optical axis (fiber and LED) lead to dissimilar and unexpected illumination patterns. For instance, figure 4.2 shows the 2-D intensity plots detected in the far field in air for the same emitter fiber (POF, 1.5 m long) and in the same conditions but with two different LEDs coupled to it. Left pattern corresponds to a 5 mm narrow angle blue (470 nm) LED [33], while the right one is due to an IR (850 nm) 3 mm LED having wider viewing angle [34]. The differences between them become evident. It is interesting to note that these differences appear in the X-Y plane, the problem lacking completely its circular symmetry.

Therefore a one-dimensional approach like the carried out in the previous chapter could be considered as a mere estimation and a more rigorous 2-D treatment is needed to understand the fiber's behaviour in depth. However, for the sake of simplicity, we will restrict ourselves to the analysis in the X axis which in spite of its simplicity leads to qualitatively valid conclusions.

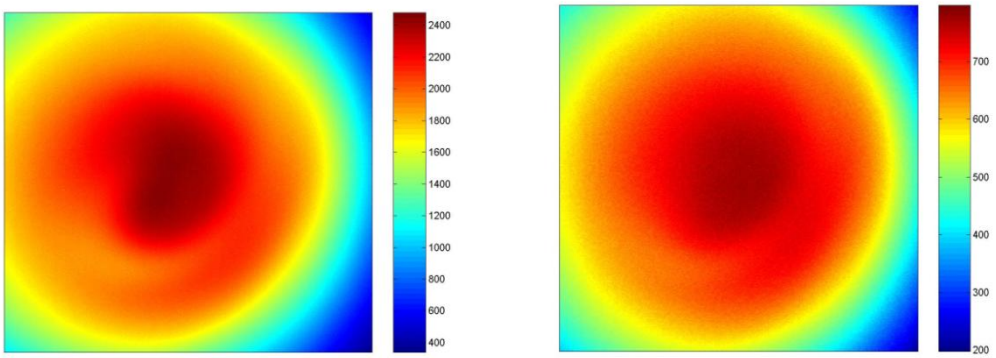

Figure 4.2. 2-D intensity plots of the same fiber coupled to different LEDs

Therefore the aim of this chapter is to study the optical fiber as a transmitter, in a way similar to the conducted before:

- For distances long enough, the emitter is considered as a point source.
- For distances short enough, the emitter is considered as an extense source (composed of point sources).

4.2 Emitter function

Following the procedure described in *'Characterization of the measuring system in transparent media'* chapter, if the emitter and receiver fibers are located far away each other the signal received by the photodiode at a given position of the scanning line is a function of the angle α that the emitter fiber (considered as a point) forms with the receiver one (also considered as a point):

$$Signal\ (\alpha) = Geometry * Fiber\ emissivity\ (\alpha) *\ R(\alpha) \qquad \text{[Eq. 4.1]}$$

where the * refers here to the pure multiplication operation and R(α), the receiver response function found before, has the form:

$$R(\alpha) = e^{-2(\frac{\alpha}{w})^n} \qquad \text{[Eq. 4.2]}$$

with parameters *n* and *w* already known. The *Geometry* term takes into account the cosine squared inverse law. According to the equation 4.1, it is possible to find the desired *Fiber emissivity* by performing a simple division operation for each position of the scanning fiber (see figure 3.4). Doing this a set of discrete values of this function can be found although the final useful form must be constructed by a continuous function fitting.

In principle, it could seem suitable to try a function similar to R(α), taking into account that both fibers are of the same kind. However the light source and the coupling method play an important role in the shape of the intensity distribution coming out of the fiber. Therefore it can be feasible to think in a function that incorporates a modulating term that takes into account the light launching:

$$Fiber\ emissivity = R(\alpha) * Launching(\alpha) \qquad \text{[Eq 4.3]}$$

The *Launching* factor should reflect all the facts influencing the distortion introduced by the (deficient) excitation of the propagating modes: misalignments, uneven filling, etc. In simple words, it will be the responsible for the lack of circular symmetry seen in the diagrams of figure 4.2. If the launching had been correct concentric circles (Gaussians when cutting in 1-D slices) would had appeared. We will construct the approximated (one-dimensional) version of this term for air and water.

4.3 Fibers in Air

If the LED and the fiber are out of alignment, it is reported that ring images appear with million-mode fibers [15]. So a function with two peaks centered at positive and negative angles would be a good candidate:

$$Launching(\alpha) = A \cdot \cos^{m_1}(\alpha - alfa_0) + B \cdot \cos^{m_2}(\alpha + alfa_0) \qquad \text{[Eq. 4.4]}$$

The following values for the parameters lead to good fittings in air:

$$Launching(\alpha) = 3 \cdot \cos^{700}(\alpha - 0.05) + 50 \cdot \cos^{3.4}(\alpha + 0.75) \qquad \text{[Eq. 4.5]}$$

This can be seen in figure 4.3 where experimental and fitted curves have been plotted together for a distance between emitter and receiver fibers of 10 mm. It can be seen that this value (10 mm) is large enough to make the point assumption valid. The LED used here and throughout the rest of the chapter has been the blue one.

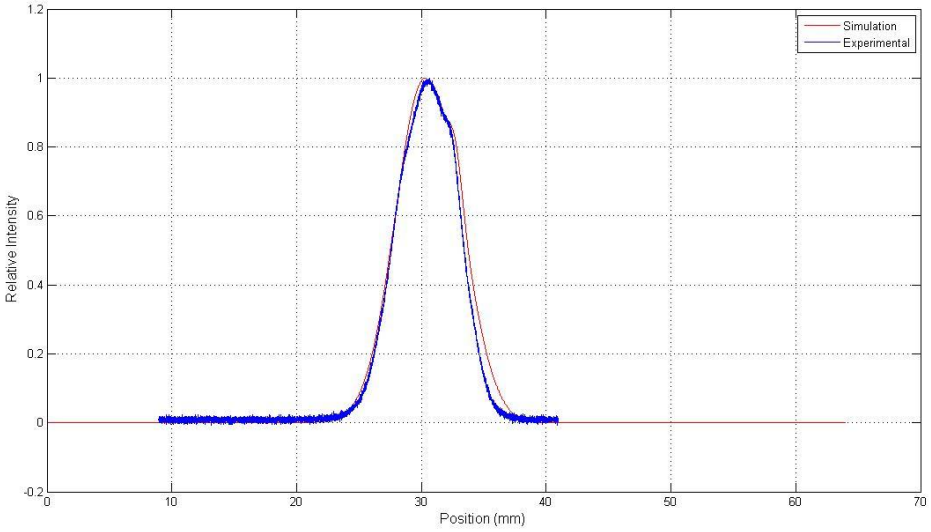

Figure 4.3. Experimental and modelled response curves in the far-field in air.

For distances shorter than ≈10 mm, where neither the source nor the detector can be considered as point devices, both should be modelled as the sum of elemental source-detector pairs and integrated over their entire areas. That is, the sign * in equation 4.1 has to be taken here as convolution instead of multiplication. The functions that describe the angular behaviours of source and detector remain the same.

In these conditions, the fittings at short distances are also quite good, as can be seen in figure 3.4 which highlights the excellent performance of the model at short distances.

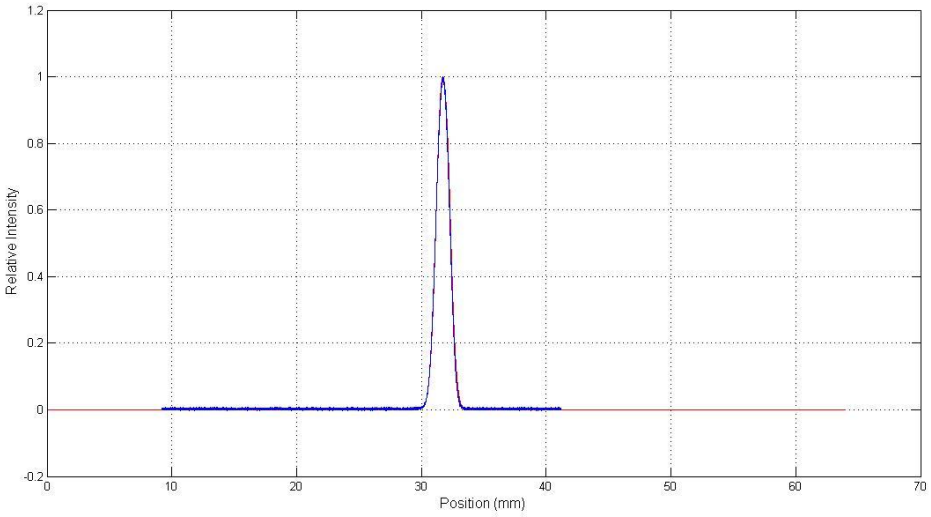

Figure 4.4. Experimental and modelled response curves in the near-field (1 mm) in air.

These good agreements in overall shape (curves have been normalized) are also kept with their absolute intensities. For instance, the ratio of intensities (this is, the areas under the curves) is 0.51 for $h = 14\ mm$ and $h = 17\ mm$ in the experimental case, and of 0.52 for the simulated one. In summary, the function defined in Eq. 4.5 adjusts accurately enough to the experimental response (see Annex 3).

As a final remark, it is instructive to compare the radiance or energy per surface unit supplied to the medium by the LED alone with that due to the same LED coupled to the fiber for two significant distances: $h = 2\ mm$ and $h = 19\ mm$. Figures 4.5 and 4.6 show these cases for LED alone and fiber respectively.

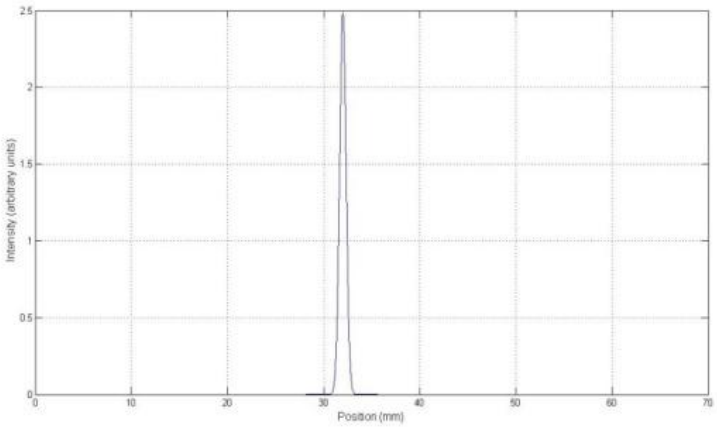

(a)

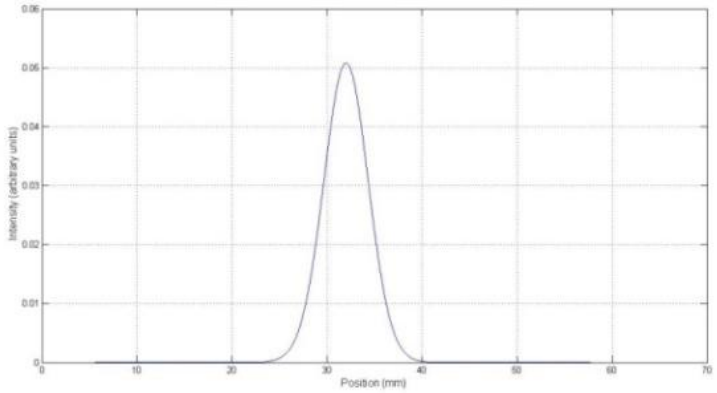

(b)

Figure 4.5 Radiance of LED at h=2 mm (a) and h=19 mm (b).

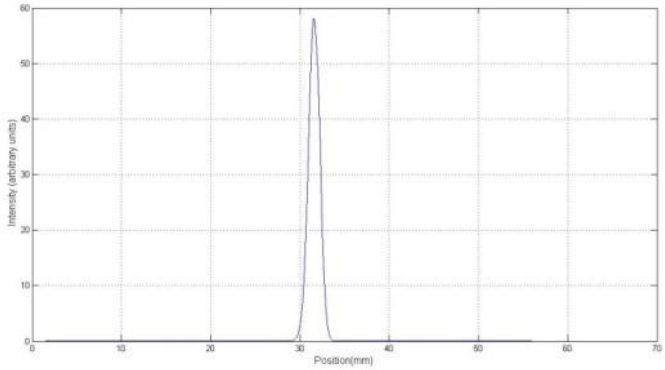

(a)

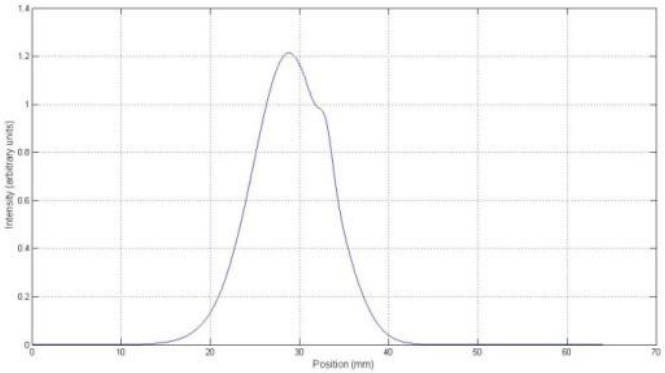

(b)

Figure 4.6 Radiance of LED + fiber at $h = 2\ mm$ (a) and $h = 19\ mm$ (b) in air.

4.4 Manipulation of modes

We have seen that the launching conditions have a dramatic effect on the light intensity coming out of the fiber. Moreover it is also well known that not all the modes launched at the fiber can propagate, even if they are allowed to do so [35]. In this section some representative examples that prove these assertions will be given, showing that an intentional manipulation of the modes can lead to different illumination patterns. And what is more important: in the majority of cases without changing the configuration of that part of the fiber in direct contact with the medium.

4.4.1. Mode filter

A multimode fiber allows a great number of modes propagating without suffering appreciable attenuation.

The number of modes, which ranges from a few tenths for narrow fibers to some millions in our case of POF, depends on the wavelength and the refraction index of the core/cladding materials [15]. Although not exactly true, one can think of these propagating modes as rays bouncing at the core boundaries at angles greater than the total reflection one, thus minimizing the energy (evanescent) that flows to the cladding and out of the fiber.

Since the total reflection conditions are based purely on geometry, it is easy to realize that bending the fiber may produce light losses due to the perturbation of this total reflection for some (high order) modes.

This fact, which is considered a drawback in fiber communication, can be exploited to eliminate some modes and to adapt the final light distribution to a specific need. Obviously this mode filtering [36] has greater impact for low propagating modes fibers than for multi-million modes fibers. The usual method to perform this filtering is by wrapping some length of the fiber around mandrels of calibrated diameters [37]. As a mere example, the light reduction effect when the fiber is bended is displayed in figure 4.7 that show the results obtained when the fiber was wrapped around a tube of 40 mm of diameter with four turns (see Annex 6 and 7). It should be mentioned that bending this type of plastic fibers with smaller diameters is difficult because of the own rigidity of the material. Otherwise, with glass fibers this action is much easier and a good number of turns can be done without further problems thus allowing a thinner tuning of the filter.

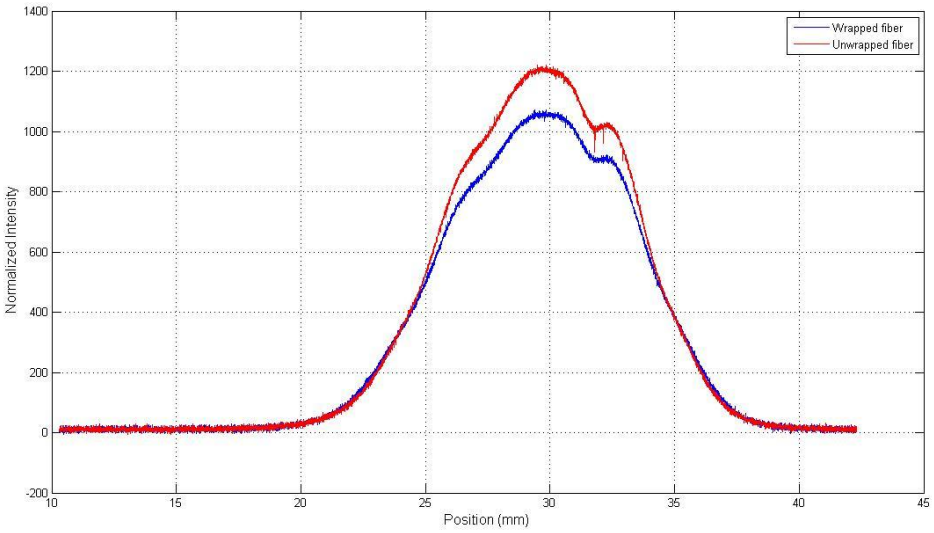

Figure 4.7. Effect of the fiber wrapping.

4.4.2. Selection of launched modes

The main factor affecting the light distribution coming out of the fiber is the LED-fiber coupling. It is possible to perform a selection of those modes excited by modifying adequately this coupling, apart from the existence of other perturbations such as mode mixing or mode scrambling [38] that spoil the initial light injection. Although these phenomena are significant for long fibers (>100 m), it is something to take into account even for short pieces. On the other hand, it is well known that POFs need lengths in excess of 1m to allow the modes cover uniformly the outer tip [15].

A qualitatively example of how the launching affects the illumination is given in figure 4.8 where the light detected for the same fiber at the same distance is displayed when the LED is "touching" the entrance tip and when it is 10 mm apart.

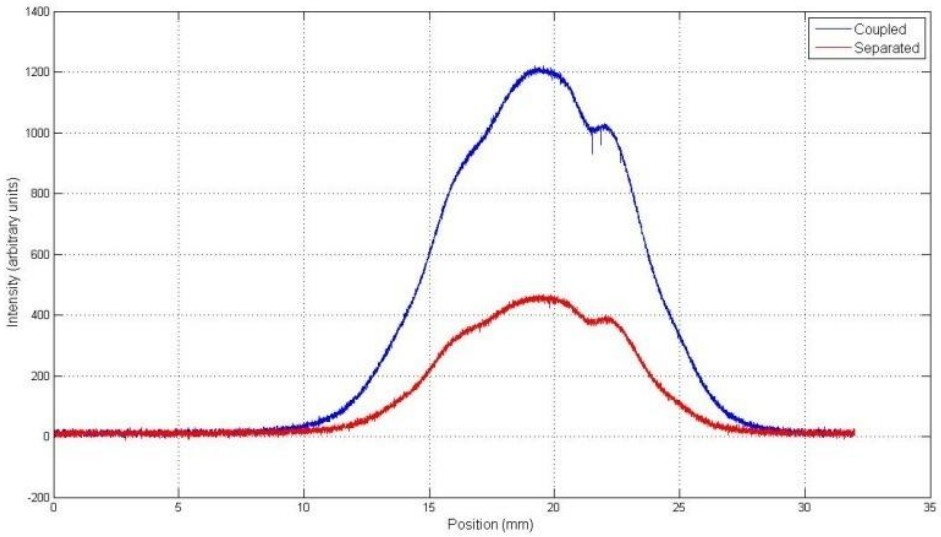

Figure 4.8. Light detected with the same fiber for two launching conditions.

4.4.3. Exotic configurations

If the LED and the fiber have their optical axis well displaced, the light "cone" that comes out of the fiber is not further a true full cone but a hollow one [39]. This is so because only those modes with angles respect to the fiber's axis greater than a given value are excited while the others, responsible for the "filling" of the cone are rejected. This is equivalent to saying that the small humps seen in the patterns of figure 4.8 evolve to two well separated peaks, like those shown in figure 4.9. This figure displays the (sliced) light pattern detected when the LED excited the fiber through an angle of 20^{o}.

Total intensity becomes in fact reduced but the illumination pattern does not retain the usual bell shape, fact that can be exploited in some applications. Peaks separation is directly related with the off-axis angle.

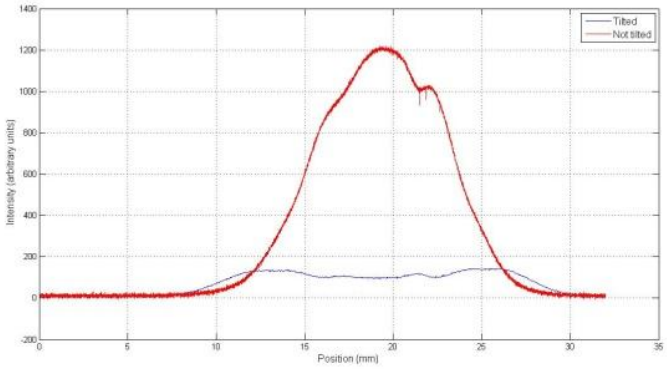

(a)

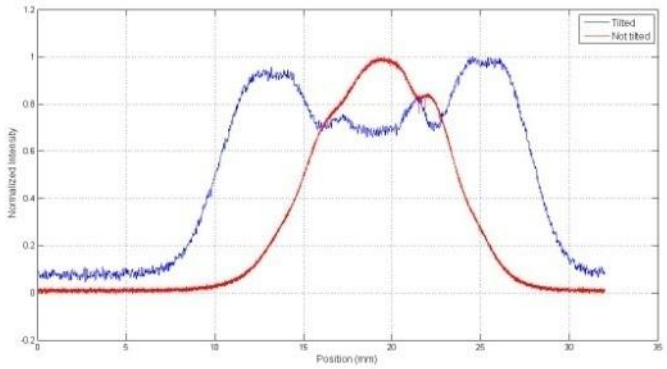

(b)

Figure 4.9. Effect of Led tilt, not normalized (a) normalized (b).

4.4.4. Exit tip

The quality and shape of the exit tip have a dramatic effect on the illumination pattern. Fiber with diameters that large (1 mm) allows the user to engrave it in the way suitable to achieve a desired light distribution. Here we have tried to get a planar, well polished surface, but other configurations are possible as well. For instance, it is possible to cut the tip in a round shape thus acting as a lens concentrating (o diverging) the exit rays [40]. It is also usual to taper the tip in order to modify the geometric aperture, making it asymmetric [41]. Another popular configuration consists in leaving the surface unpolished in such a way that it acts as a diffuser, thus widening the light cone [42].

Even some high-tech solutions have been attempted aimed at eliminating most of the non-fundamental modes by means of destructive interferences in irregularities of the surface developed by etching [41, 42].

As a mere example, we will show how the elimination of some region of the unevenly polished tip (because this process has been made by hand) lead to somehow different light patterns. Figure 4.11 shows the comparison of the normalized intensity distributions for several distances when the exit tip has been partially covered with black tape (upper) and when the entire surface contributes to the illumination (lower).

Since the tip is not homogeneous, the covered part would throw light in a way different to the uncovered and thus the patterns become slightly different, what is indeed a verification that the hand-polishing is not too bad (see Annex 5).

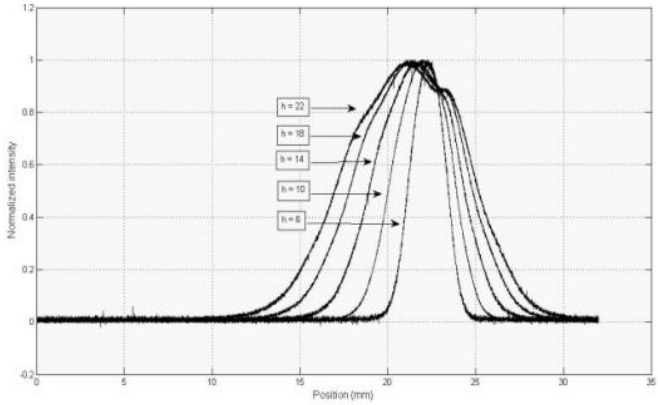

(a)

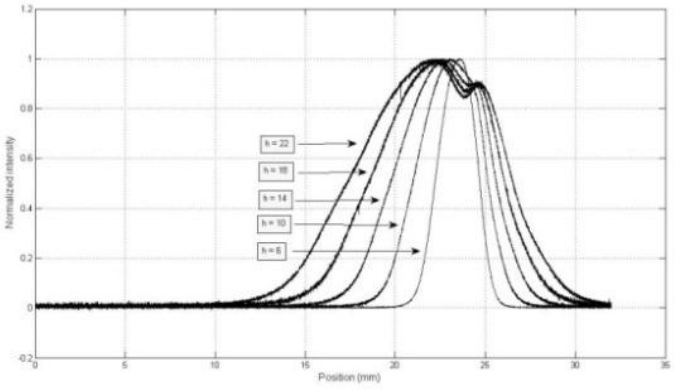

(b)

Figure 4.11. Comparison between illuminations due to partially covered (a) and uncovered (b) exit tips.

4.5. Fibers in Water

Assuming that the function $R(\alpha)$ has the form found before for the water (super-Gaussian with n=3 and w=0.3), it would only remain to find the corresponding *Launching* function. It results like the equation 3.5 although with slightly modified parameters, reflecting in some way the "attenuation" of the launching errors introduced by a denser medium:

$$Launching(\alpha) = 4 \cdot \cos^{700}(\alpha - 0.05) + 50 \cdot \cos^{36}(\alpha + 0.1) \qquad \text{[Eq. 4.6]}$$

The goodness of the fitting can be seen in figure 3.11 for near field (left) and far field (right). Note that the humps at the right part of the curves, quite evident in the air case, almost disappear here (see Annex 4).

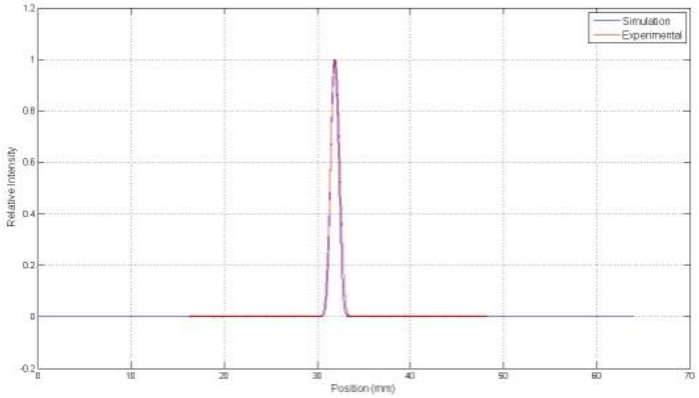

(a)

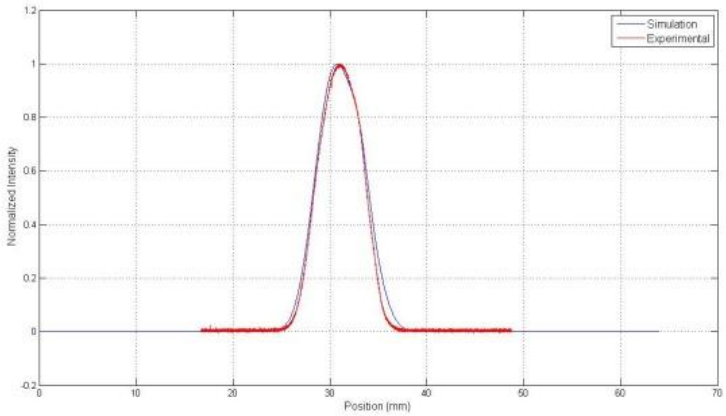

(b)

Figure 4.4. Experimental and modelled response curves in the near-field (2 mm, a) and in the far field (14 mm, b) in water.

Finally, in a way similar to the plotted in figure 4.6, we plot the energy per surface unit that the fiber supplies to the water for two distances, near and far, between emitter and detector, figure 4.12.

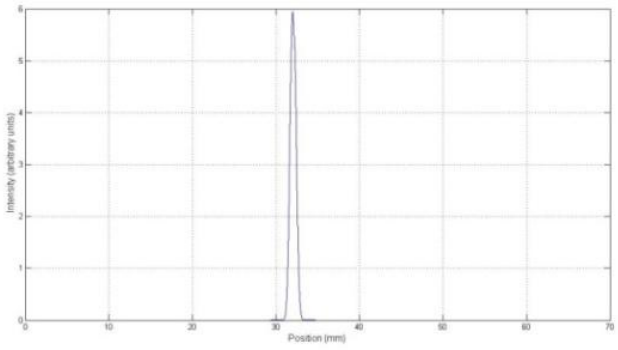

(a)

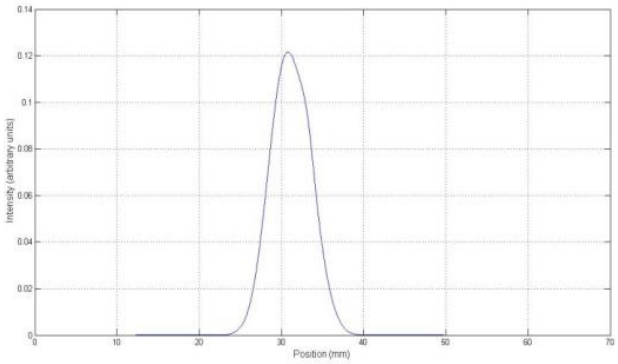

(b)

Figure 4.12. Radiance of LED+fiber at h=2 mm (a) and h=19 mm (b) in water.

4.6 Discussion

A large diameter optical fiber with millions of propagating modes along lengths in excess of 1 meter produces an almost perfectly even light distribution at the exit tip. This justifies the validity of the assumption that any point at this surface behaves like an isolated emitter with the identical intensity angular distributions. Such an assumption has been experimentally proven in this chapter, showing that the coupling LED-fiber is of great importance and that it can be modelled as a factor modulating the pure, full excited fiber.

Operation with turbid media. Forward configuration

5.1 Introduction

Once the system has been characterized using transparent media, we are going to use it to show its features when dealing with turbid media. In this chapter we will focus on the forward operation, i.e. the receiver has been place in the forward semi-sphere with respect to the transmitter, while the backward operation will be addressed in the next chapter.

Turbid media of biological interest has a refraction index approximately similar to that of water. This could justify the assumption that the fiber's response with these media adopt the form found for the water in the before chapters. However, turbidity imposes two additional constraints to the light propagation:

1. Absorption, where the beam is attenuated (or, in other words, light intensity lowers).
2. Scattering, where the beam changes its direction.

That is, the straight and lossless paths assumed until now are not realistic. It is interesting to treat these two situations separately. Media in which scattering phenomena predominate over absorption (*Highly scattering media*) will be considered first, uncovering their counterintuitive behavior. In contrast, we will show how media in which no apparent deviation of the light beam is evidenced (*Highly absorptive media*) behave in a way formally similar to the predicted for water.

5.2. Highly scattering media

5.2.1. Milk

Milk is a clear example of scattering medium due to the tiny fat droplets solved in the water. Fatty milk contains more droplets of fat while skimmed milk has a lower concentration of such particles. So, higher light extinction (scattering + absorption) would be expected with the former than with the latter.

For instance, figure 5.1 shows this light extinction for both types of milk and a mixture of them as well. Clearly the fatty one is the least transparent, this difference being more acute at IR wavelengths.

Here we are also interested in the geometry characteristics of the light thrown by the transmitter fiber to the milk in which it is immersed. As expected, this geometrical response is rather complicated and difficult to interpret and by no means similar to the obtained with water. In effect, figure 5.2 shows the plots obtained at two extreme positions (one with both fibers almost touching and the other with them well separated), together with the pattern expected from water. It is worthwhile to note that the profiles of skimmed and fatty milks are almost coincident for short paths and become frankly dissimilar at long distances.

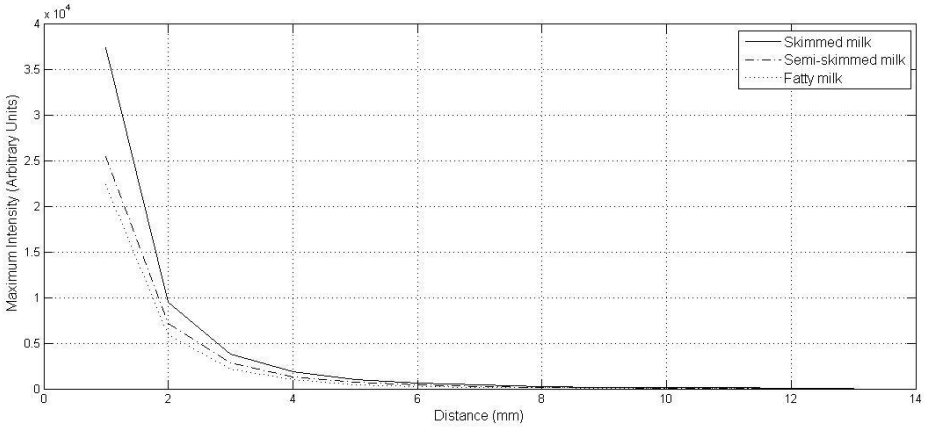

(a)

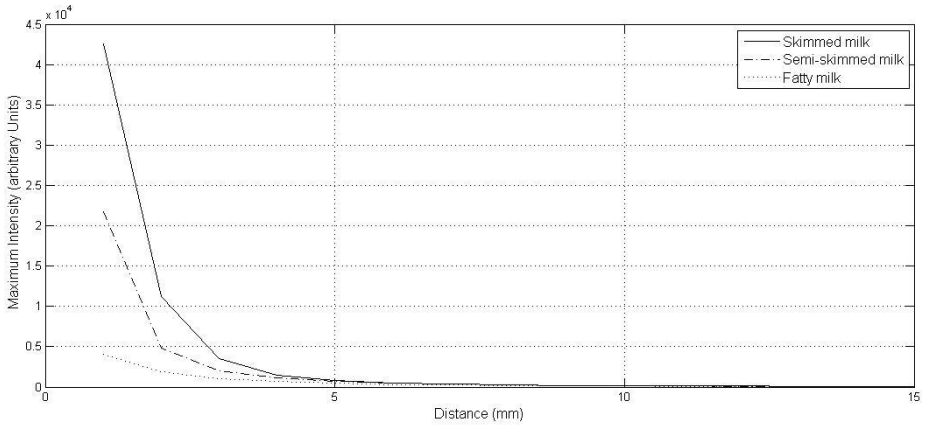

(b)

Figure 5.1 Absorption of milk at 490 nm (a) and 850 nm of wavelength (b).

Milk always produces wide bell-shape curves, much wider than the water, even when the path of the light is short (at distances $h \approx 1\ mm$).

This would lead to deduce that the effect of the scattering is so acute that the light immediately exiting the transmitter fiber is not further confined to the cone defined by the geometrical aperture but spreads over larger angles. Reciprocally, the light reaches the receiver within an aperture abnormally large. This peculiar behavior has been confirmed with our simulation model for water (in 'Characterization of the optical fiber as emitter in transparent media' chapter) if we force the reception and emission angular functions to follow an almost isotropic dependence. The matching is notoriously good at any distance.

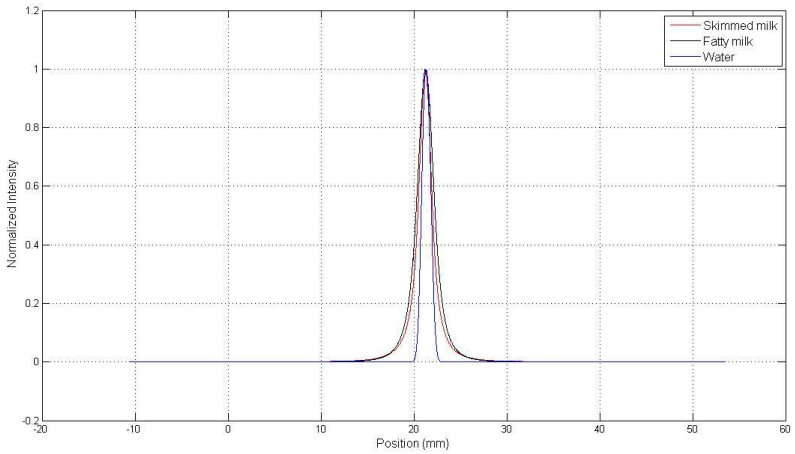

(a)

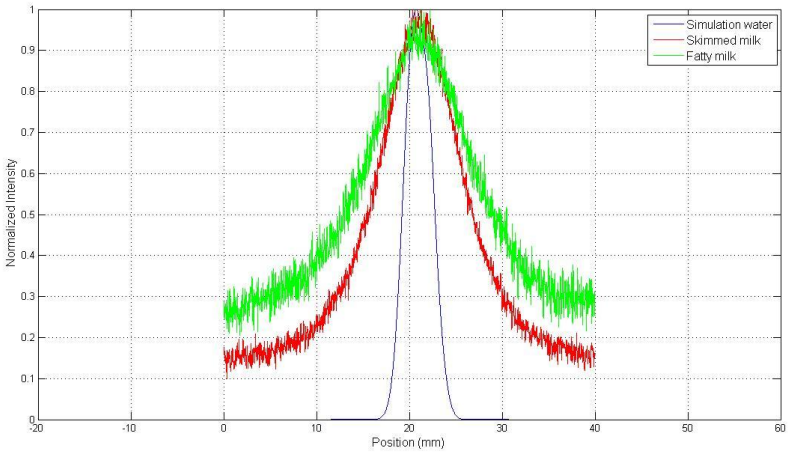

(b)

Figure 5.2 Normalized responses to milk and water at distances h=1 (upper) and h=12 mm (lower).

Obviously this does not constitute a faithful reproduction of the reality. In truth, light does exit and enter the fibers through their actual cones and, since the scattering is so important, it rapidly deviates from the straight line resulting in an illumination (and reception) diagram that resembles a uniform emission. The theoretical treatment of this problem is rather complex and should be done with the aid of numerical techniques (Monte Carlo, random walk, the diffusion equation… [45]), beyond the scope of the present work. Rigorous analytical approximations can be found elsewhere dealing with the solution of the *Radiative Transport Equation* [46]. There, it is assumed that light passes though a scattering cloud and reaches an observer *outside* the cloud. Here, both the source and the "observer" are *inside* the cloud.

5.2.2 Milk with an obstacle

The consequence of strong light scattering can be graphically appreciated by interposing a small obstacle between the emitter and receiver fibers. Figure 5.3 sketches the top view of the obstacle (in red) placed at a distance (normal to the drawing plane) of 5 mm from the emitter tip (blue). The obstacle is 1.8 mm wide and covers approximately one half of the blue fiber.

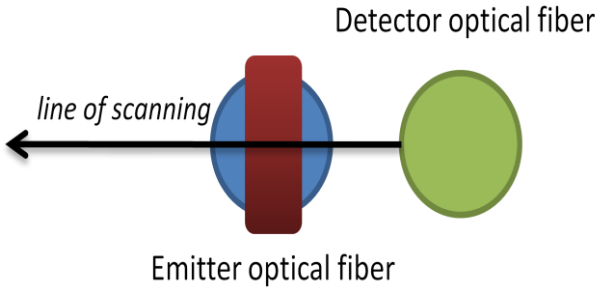

Figure 5.3 Top view of the placed obstacle.

The responses of the system with the obstacle for different media are displayed in Figure 5.4. As we can see, for the cases of air and water the familiar bell-shape patterns have been "cut" by the obstacle, forcing the intensity to zero. On the contrary, when the light propagates through the milk the obstacle makes the intensity diminish when the scanning fiber passes over but without zeroing it.

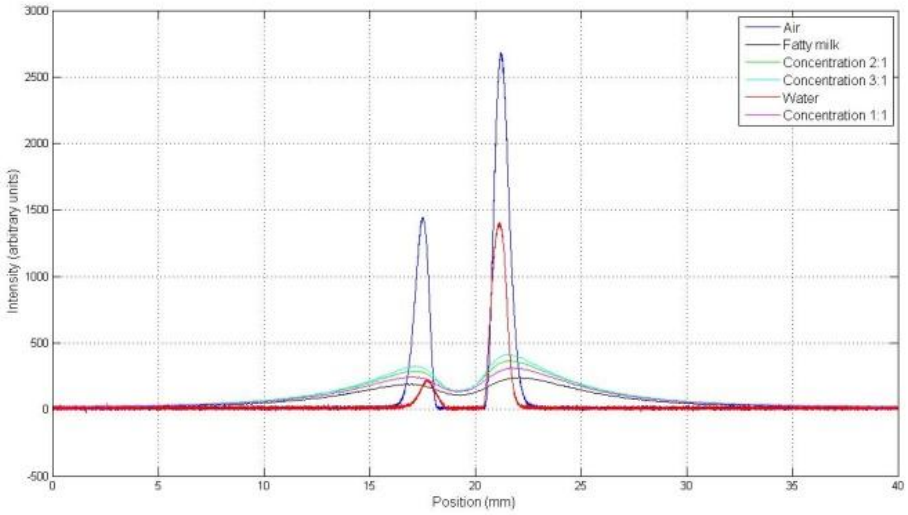

Figure 5.4 Response of the system to the obstacle for different concentrations.

Concentration 1:1 corresponds to a solution composed of 10 ml of water and 10 ml of fatty milk; concentration 2:1 corresponds to 20 ml of water and 10ml of fatty milk, and so on. It is important to remark that the light (LED current) that illuminated the milk was 5 times more intense than the used with air and water. Therefore the actual sizes of the milk curves in relation to the others are even smaller than the showed in the plots.

It is straightforward to include the effect of this obstacle in the MATLAB codes that simulate the performance of the system (see Annex 8). This modification works fine for air, water and other liquids with weak scattering (see below), but fails when applied to milk. In fact, if we accept that the almost isotropic approximation formulated in Section 5.2.1 remains valid and proceed to run the code with the obstacle, the pattern of figure 5.5 follows, curve that does not correspond with the reality (figure 5.6). This proves the inaccuracy of that approximation and reinforces the need of a numerical approach to the problem.

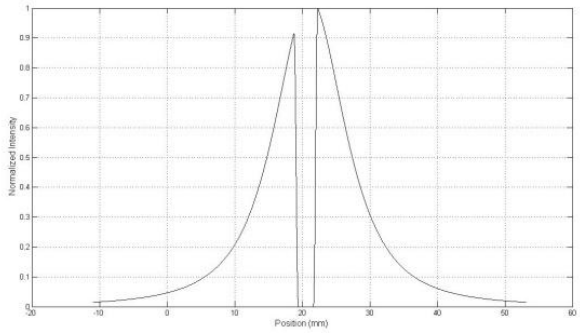

Figure 5.5 Simulation of the response for a distance of 11 mm between fibers.

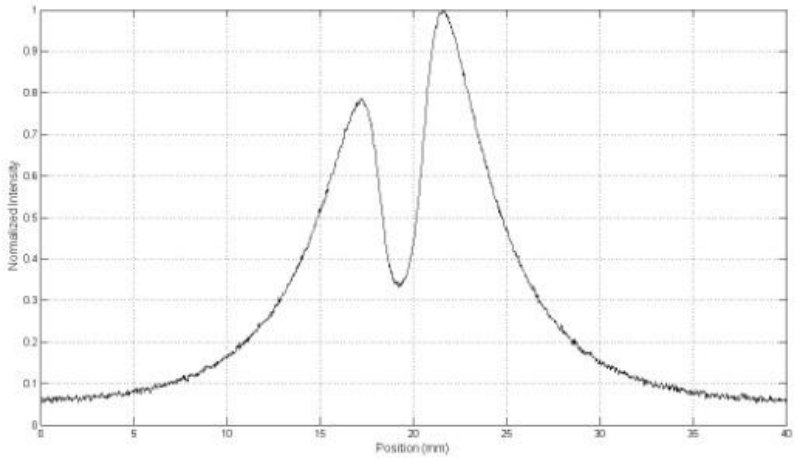

(a)

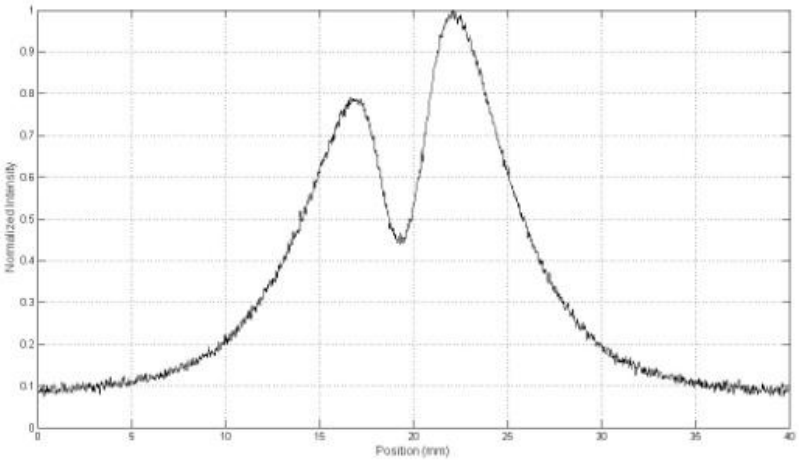

(b)

Figure 5.6 Response for skimmed milk (a) and fatty milk (b) to the obstacle at a distance $h = 11\ mm$.

5.2.3 Blood

Blood is another example of scattering medium. In this case, the responsible are the Red Blood Cells (RBC) present in the water-like solvent. Due to its evident biological importance its properties (optical included) have been extensively studied and there are plenty of references to the blood's parameters in the literature [47]. Here we have focused on its absorption and scattering characteristics and in particular on how they affect the shape of the response patterns, rather than on the different IR absorption of hemoglobin depending on the oxidation state.

Blood was obtained from mice's tails and diluted in water in a 1:10 proportion. The blood used was venous blood relatively deoxygenated. Two LEDs have been used to excite the sample: blue (peaked at $\lambda = 490\ nm$) and IR (peaked at $\lambda = 850\ nm$).

This represents two limit bands in the visible and the important zone of the IR. From [48], the ratio between scattering and absorption coefficients for undiluted blood is of the order of 2 at the first wavelength and 1000 at the other.

In these conditions, a scanning of the illuminating fiber has been performed without any obstacle interposed between the fibers. Figure 5.7 shows the resulting plots, together with the corresponding to pure water taken with the blue LED. A remarkable feature of these patterns is the similarity in shape between the blood and water curves when the former is illuminated with blue light. On the contrary, the IR light makes the curve widen and its bell-shape deform, clear consequence of the higher scattering contribution in the IR band even at this relatively low concentration. However, this curve, although being sensibly narrower than the one due to the (skimmed) milk, bears a resemblance to a top-hat instead of the sharper and bell-like curves of figure 5.2. This can be considered as a proof of the different overall effects of scattering in both cases (probably simple vs. multiple direction changes [49]).

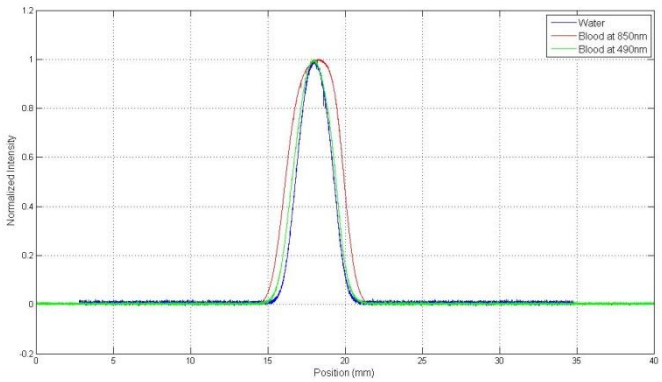

Figure 5.7 Normalized responses of blood as medium at different wavelengths at h = 3.

5.3. Highly absorptive media

5.3.1 Coffee and Vinegar

When the absorption prevails clearly over the scattering the slight distortion seen for the blood at blue wavelength disappears and only a net signal reduction is observed, the curves keeping essentially their shapes.

It is appropriate to carry out the study of the entire Section 5.3 with the obstacle interposed between the source and the receiver (at 5 mm from the former one), because this imposes an absolute reference to the problem.

Vinegar and soluble coffee are two liquids with very small scattering coefficient [50]. Figure 5.8 shows a comparison of these substances – two different concentrations for the coffee and the vinegar directly from the bottle – with air and pure water. It is seen that only the soluble coffee at high concentrations presents some scattering, although not significant compared to milk. The others do absorb light but without dispersing it.

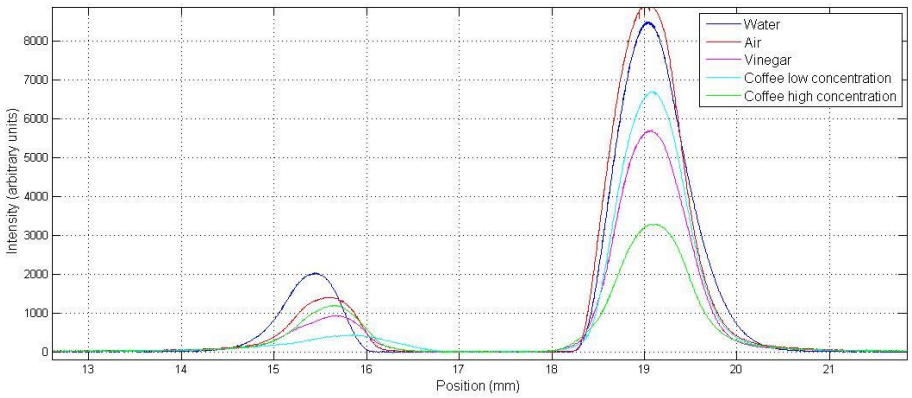

Figure 5.8 Response for air, water, vinegar and coffee at h=19.

5.3.2 Cola

From the optical point of view, coke is basically an intimate solution of some substances in water and not an emulsion. Since there are not free scattering centers, all the light extinction comes from pure absorption. This will be studied in detail for two concentrations of cola in water, 1:1 and 1:2. Blue LED ($\lambda = 490\ nm$) has been used to illuminate the mixtures.

Attenuation coefficients were calculated after the implementation of the Beer-Lambert Law [51] for absorption in the model (see Annex 9). These coefficients have been deduced by comparison of the patterns of coke with that of pure water and using the value of this last one as reference (μ_a =0.01 mm^{-1}).

In this way, the following data hold: for cola mixed with water in a 1:2 solution, μ_a =0.02 mm^{-1}; for cola mixed with water in a 1:1 solution, μ_a=2 mm^{-1}. The model matches quite well the experimental response (figure 4.9), because of the insignificant role that the scattering plays.

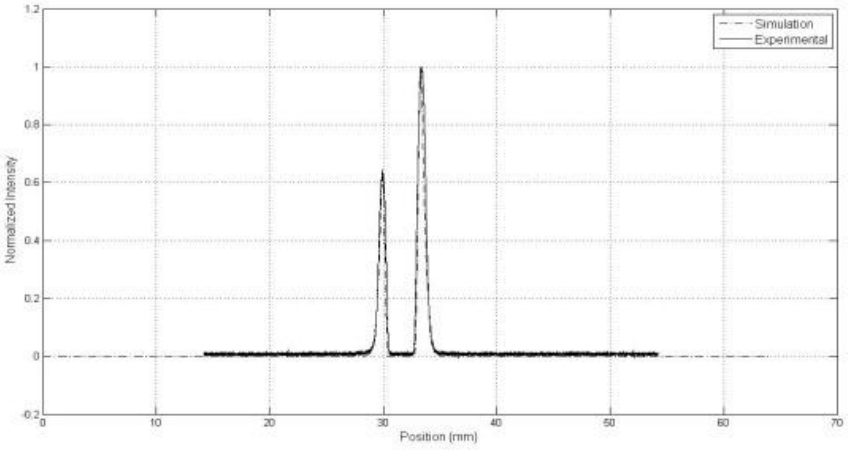

(a)

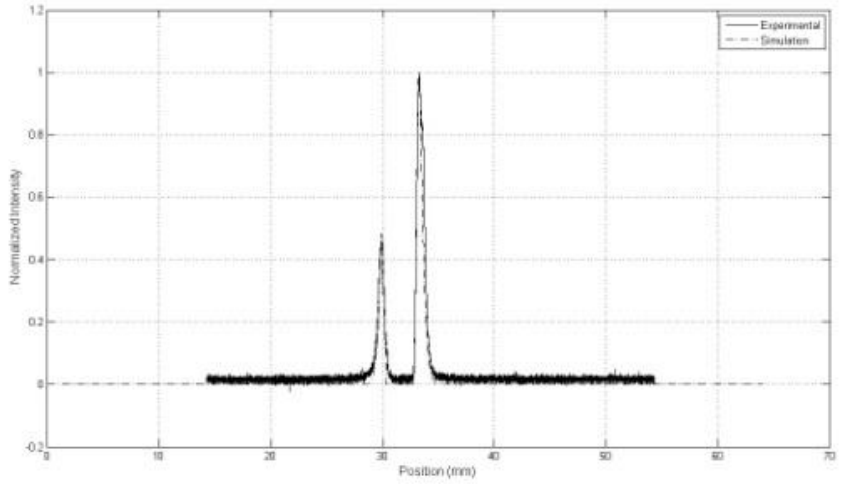

Figure 5.9 Experimental and fitted output curves for cola at concentrations 1:2 (a) and 1:1 (b) at distances emitter-receveiver of $h = 12\ mm$.

5.4. Meat

Until now, liquids have been used as propagating media. But light also penetrates in not completely opaque solid substances, like tissues. In fact these media are the most important from the biological point of view. Therefore, we have tested the system with a special type of tissue: fresh meat.

In a first experiment, we have replaced the opaque obstacle used before by a thin 3 mm slab of pork. So, the light can go through the obstacle suffering the familiar effects of absorption and scattering.

The surrounding medium has been cola, that it is known acts as a kind of “digester” due to its high carbonic acid content [52]. This transformation process implies some dilution of meat in the cola (shrinkage) as well as a changing in the optical properties of the slab, turning darker. In Figure 5.10 we can see how the response of the system to the meat obstacle changes as a function of time. As time passes, intensity is lowered and the shape of the distribution changes due to the degradation process, this change being more acute in the first hour and essentially stable after 2 hours.

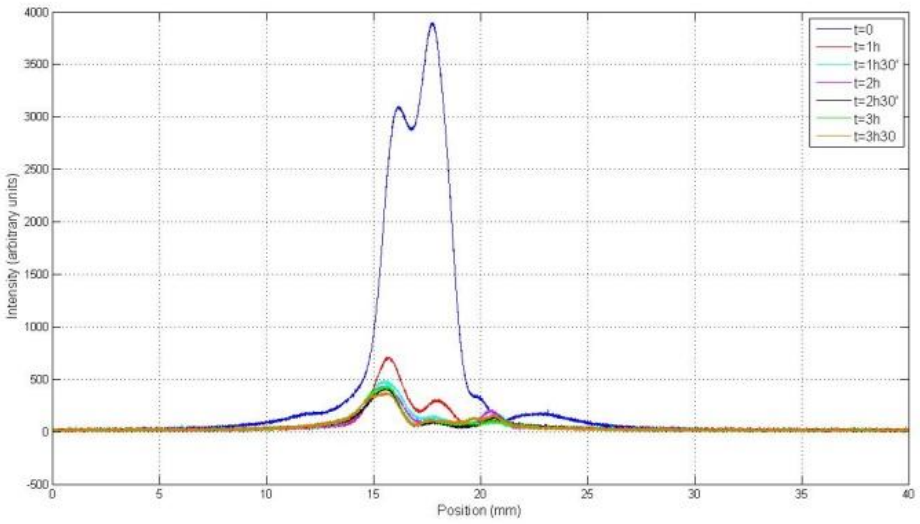

Figure 5.10 Meat degradation due to cola digestion as a function of time.

This figure also highlights other important characteristics of tissues as opposite to liquids. They are generally inhomogeneous, that is, not every point within the illumination cone absorbs (or scatters) in the same way, thing that uses to happen when the liquid is a homogeneous solution. For instance, the initial curve (t=0) presents two peaks of dissimilar heights because the light intercepts a nerve of the pork meat, nerve that seems to evolve in a different way when attacked by the cola (peaks for t>1 h are interchanged).

In a second experiment, three slabs of approximately equal thickness 2 mm of beef meat, pork skin and animal fat have been placed just on the transmitter fiber (touching its tip) in air and the scan was performed at a distance $h = 1\ mm$ the fiber being excited by an intense light source. The comparison among the different absolute responses is given in figure 5.11. The three curves are wide enough to deduce a strong influence of scattering.

The green one (fat) reflects in addition some irregularities due to wrinkles; the other two patterns are symmetric as corresponds to pieces essentially homogeneous. Moreover, fat absorption is higher for the same conditions than meat and pork skin.

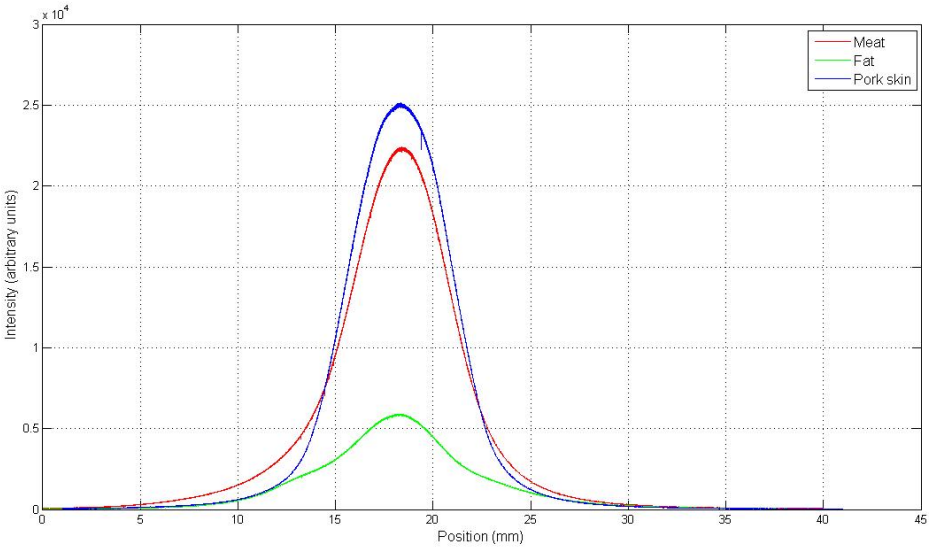

Figure 5.11 Response to three slabs of different kinds of meat.

5.5. Discussion

Light from the emission fiber propagates in the forward direction through turbid liquid or solid-like media suffering absorption (reduction in energy) and scattering (deviation from straight paths). This distorts the map of the energy that the medium receives in a rather complicated way. If there were only absorption, the illumination (and reception) cones from (towards) the fiber remain essentially similar to the defined for water, although with reduced intensity. If the scattering is acute (as in most biological samples), severe deviations may occur, difficult to predict analytically due to the fact that the illuminator is immersed in the scattering medium. It a very first approximation and with severe scattering, things seem to behave as if the light cone (defined by the geometrical aperture) widens abnormally until becomes an almost isotropic emission.

An important difference between scattering and purely absorptive media is the possibility of precise locating objects inside the last ones; something that requires advanced inverse methods if applied in scattering media.

6.1 Introduction

'Characterization of the measuring system in transparent media' chapter focused on the forward operation, placing the receiver in the forward semi-sphere with respect to the emitter. 'Characterization of the optical fiber as emitter in transparent media' chapter, on the contrary, will focus on the backward configuration. For that, detector and emitter fiber are aligned and only the detector will follow the line scanning while the emitter will stay fixed as shown in Figure 6.1. Reflection of light will rule the response of our system [53]. For opaque materials used as target materials, specular reflection will govern the output intensity. For non-opaque (turbid) materials (such as skin, meat, emulsions…) light will enter the material and bulk diffusion reflection will direct the response [54].

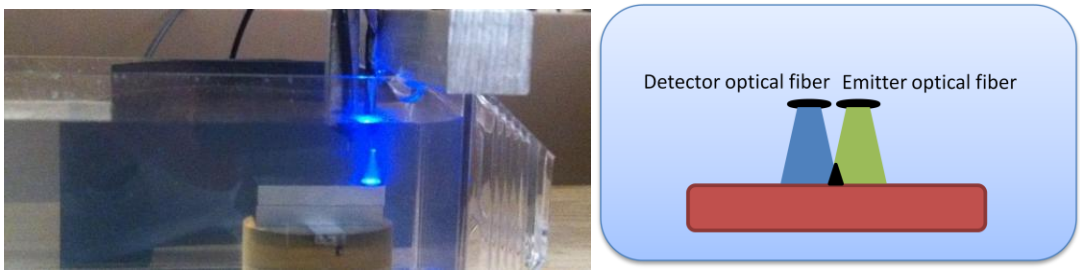

Figure 6.1 Backward configuration of the system. Real system (left) and ideal scheme (right).

As we can see in the real system displayed Figure 6.1, light is reflected in an opaque medium. Emission and reflection by optical fibers is done by cones which overlap differently at different heights (scheme of Figure 6.1, for a given height). Overlapping of cones and horizontal scanning of the detector optical fiber at different heights allows the analysis of bulk backscattering and formation of 2D images.

6.2 Opaque target in different media

Experimental response for a light source of a wavelength 490nm with an opaque medium (polished metallic piece) is displayed in Figure 6.2 for a linear scanning of the detector with a fixed emitter. As we can see, distributions show irregularities due to the non-ideal surface of the material under study.

Thanks to the concentration of rays produced by water (even if cones of fibers are narrower), intensity increases in comparison to the result obtained with air. The same behavior is obtained for the case of a LED of 850nm used as light source.

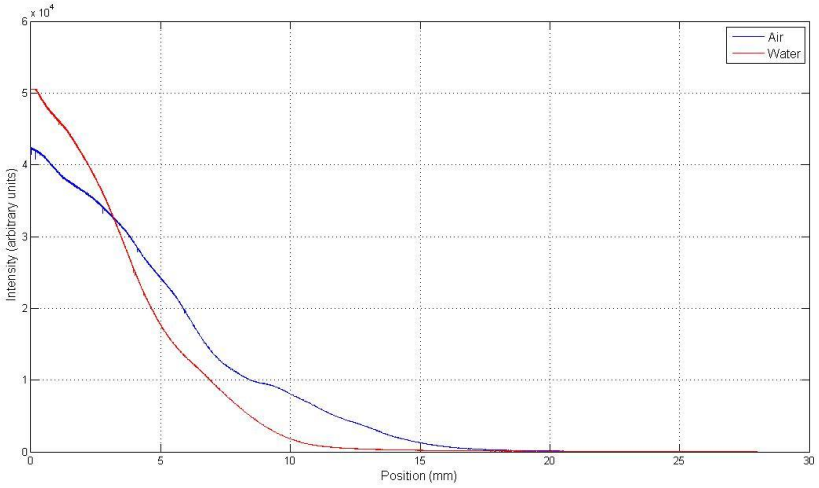

Figure 6.2 Line scanning response of an opaque material in air and water medium.

As done in the 'Characterization of the measuring system in transparent media' chapter, study of responses of opaque materials to light, in backward configuration, was done for fatty milk and skimmed milk as media for $\lambda = 490\ nm$ and $\lambda = 850\ nm$. The target metallic piece used was the same than the one used in Figure 6.3. A specular reflection study in water (transparent medium) and milk (scattered medium) media was done.

At this wavelength $\lambda = 490\ nm$ and as height increases, water absorption in comparison with fatty milk and skimmed milk absorption varies as shown in Figure 6.3. For $h = 4\ mm$, water absorption is lower than in the case of skimmed milk, and this last lower than in the case of fatty milk, as expected from results obtained in 'Characterization of the measuring system in transparent media' chapter. However, when the target is placed at $h = 13mm$, absorption is reversed and water absorption becomes higher than the one of fatty milk. Finally, for h=21 mm, water absorption turns lower as was the case at low distances.

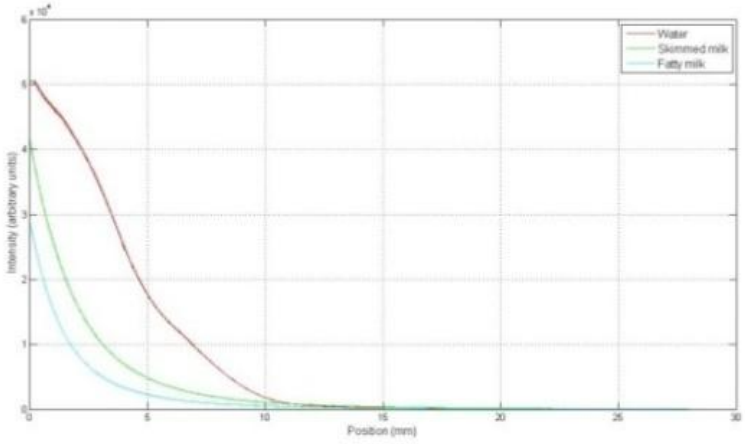

(a)

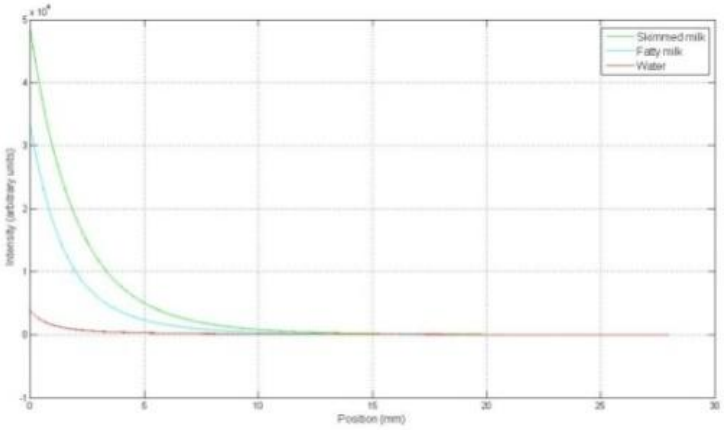

(b)

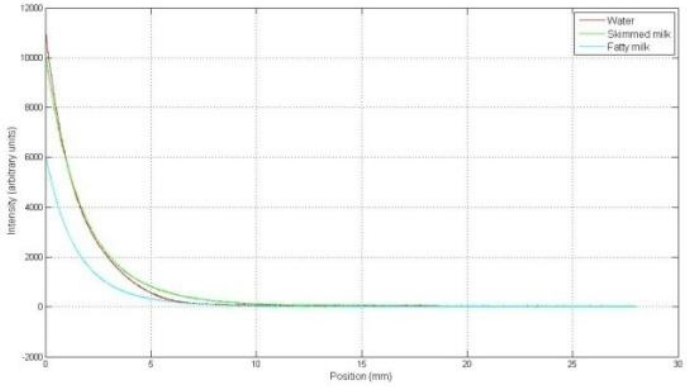

(c)

Figure 6.3 Water, skimmed milk and fatty milk absorption at $\lambda = 490\ nm$ for $h = 4\ mm$ (a), $h = 13\ mm$ (b) and $h = 21\ mm$ (c).

For the case of wavelength in the IR ($\lambda = 850\, nm$), absorption of fats changes as expected from its absorbance coefficient spectra [55]. For any height, absorption of fatty milk is lower than absorption of skimmed milk. Water behavior at low distances is the same than in the case of $\lambda = 490\, nm$. However, at high distances $h = 21\, mm$, original behavior is not recovered again as displayed in Figure 6.4.

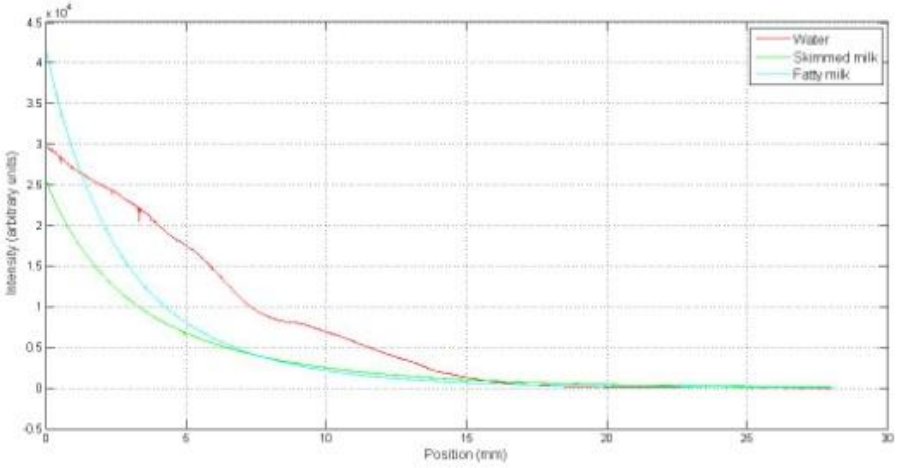

(a)

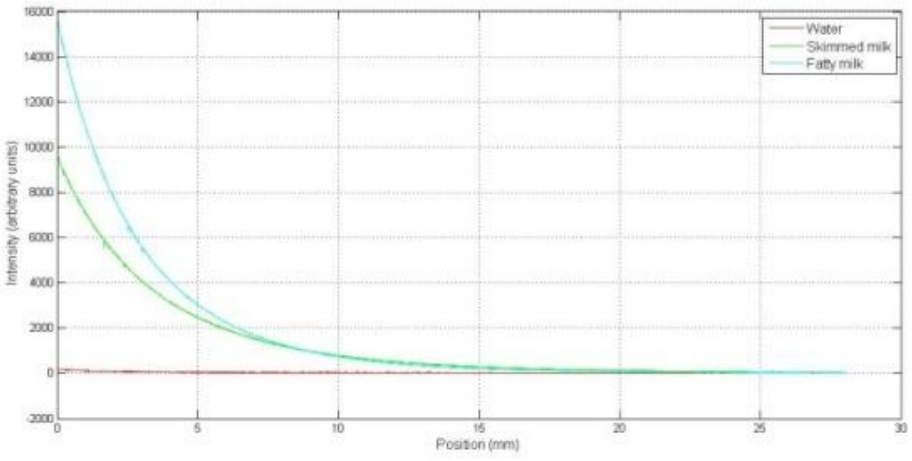

(b)

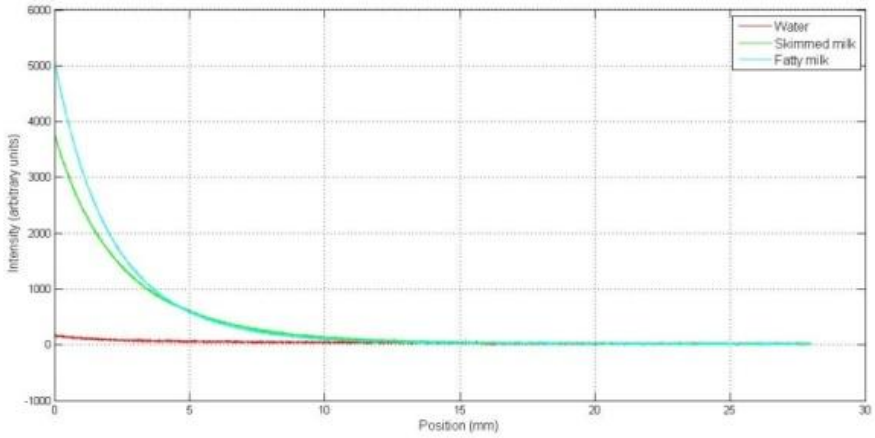

(c)

Figure 6.4 Water, skimmed milk and fatty milk absorption at $\lambda = 850\ nm$ for $h = 4\ mm$ (a), $h = 13\ mm$ (b) and $h = 21\ mm$ (c).

As we can deduce from the results obtained, scattering in the backward configuration determines the output response (even more than in the forward configuration). The geometry of the system and so, path of light, is now more complex than in the previous configuration. Rays travel from the emitter to the target material through the medium, reflect and travel back to the receptor optical fiber in the same medium. If this medium is a highly scattering media (fatty milk) responses are variable, and the radioactive transfer equation (RTE) needs to be applied in order to model radiance distribution.

6.3 Solid-like turbid media

In order to study the behavior of solid-like turbid media, three different fresh meat were used as target (chicken, pork and cow meat) [56]. For this study, emitter fiber was placed in direct contact with the meat portion, while the detector fiber moves in the horizontal line scan. Emitter optical fiber, receptor fiber and the thick portions (≈5 mm thick) of meat where immerse in air first, and in water secondly.

Response when the meat is immerse either water or in air, or at wavelengths of 490 nm or 850nm for the three fresh slabs is the same; water absorption is lower than in the case of air as expected from results obtained in 'Characterization of the measuring system in transparent media' chapter, displayed in Figure 6.5 (only response when using chicken as target immersed in water or in air at 490 nm).

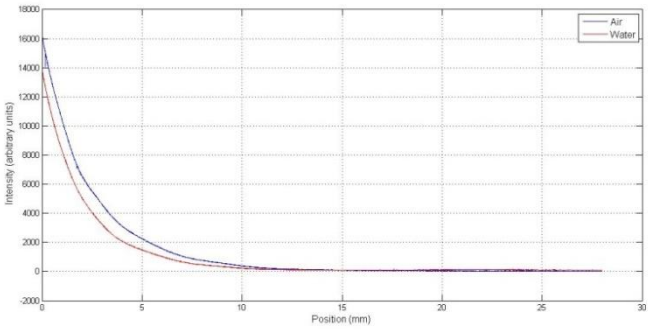

Figure 6.5 Response using $\lambda = 490\ nm$ for chicken as target immersed in water or air.

Extinction of the three slabs varies as a function of the wavelength used. For the case of $\lambda = 490\ nm$, chicken extinction is lower than the one of the pork or cow. However, in the case of $\lambda = 850\ nm$, higher extinction is experimentally found for pork rather than in chicken and cow slabs, as displayed in Figure 6.6 in air as medium [57]. Moreover, extinction of light is higher at $\lambda = 850\ nm$ (this is, output intensity is lower) than for $\lambda = 490\ nm$ for any of the slabs used.

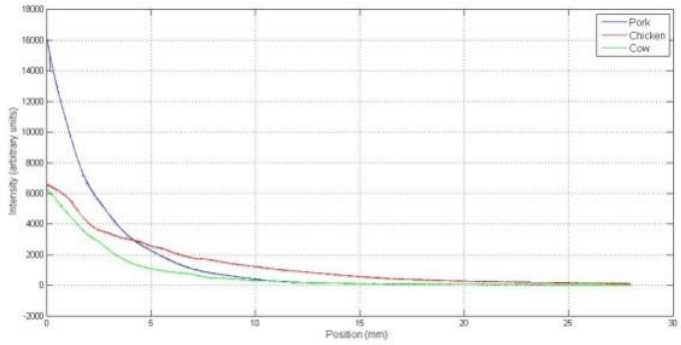

(a)

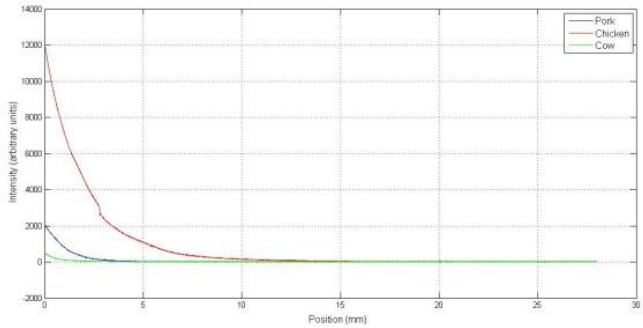

(b)

Figure 6.6 Absorption of chicken, pork and cow for $\lambda = 490\ nm$ (upper) and $\lambda = 850\ nm$ (lower) in air.

6.4 Emitter and receiver linked – surface study

1D

In section 6.1, a system based on a mobile receptor fiber and a fixed emitter fiber was described and analyzed for different targets in different media. Now, in order to study the surface of a given material, receptor fiber and emitter fiber will be linked and will move horizontally. By using an opaque target, a vertical scanning would follow the response observed in Figure 6.8a. Starting from 0 (detector and emitter cones do not overlap at h≈0) intensity increases as height gets bigger, since cones of the fibers overlap augmenting the area of slab intersected ($a_2 > a_1$), until a maximum is reached as shown in Figure 6.7.

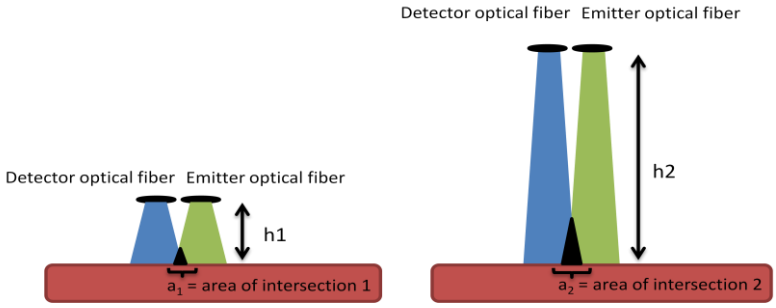

Figure 6.6 Scheme of intersection area variation as a function of the distance between fibers and target.

Immediately after this maximum, distribution lowers until light is not longer perceived since bulk diffraction applies stronger as height increases. This behavior is well-studied and used in fiber optics displacement sensors [58]. However, for the case of a turbid material as target, the curve does not starts at 0, since light is transmitted into the material and scattered due to a complex microstructure so that backward scattering produced by the particles encountered are already perceived by the detector fiber as displayed in Figure 6.8b (reflection and refraction). The behavior as height increases follows the same rules as in the case of an opaque target.

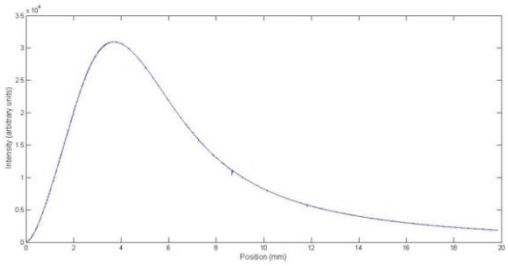

(a)

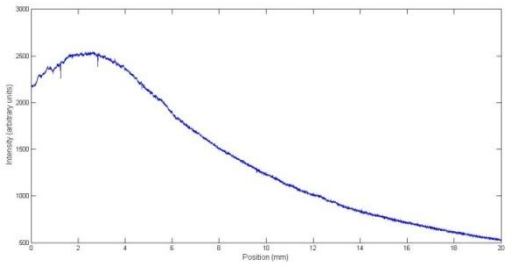

(b)

Figure 6.7a Response of a vertical scanning in backward configuration of an opaque material used as target. 6.7b Response with the same configuration for a non-opaque material.

In order to study the surface of the slabs, as previously mentioned, emitter is configured so that it follows the movement of the detector fiber in the line scanning as well. For that, both the slab and the fibers were, firstly studied in air as medium and secondly studied immersed in water. Experimental results are displayed in Figure 6.8.

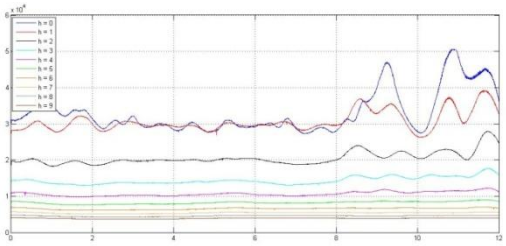

(a)

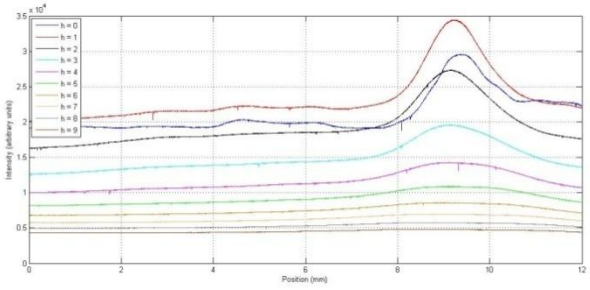

(b)

Figure 6.8 Surface study of a slab of cow muscle in air medium (upper) and immersed in water medium (lower) at different heights.

As we can see in Figure 6.8, as height increases, roughness details are lost since resolution decreases (same overlapping of cones but higher area of intersection at different heights).

And roughness is easily detected when the slab is not immersed in water but in air. This is due to the fact that the index of refraction of air ($n_a \approx 1$) in comparison with the one of the slab ($n_s \approx 1.46$) so $n_s >> n_a$, higher than the difference between the index of refraction of water ($n_w \approx 1.33$), $n_s > n_w$ following Fresnel equations [59]. For a better understanding of this fact, 2D images were obtained and are discussed in the next subsection.

Is important to notice that for the case of water as medium, intensity at h=0 is lower than the one obtained at h=1, this is due to the behavior described following Figure 6.7b. Reflection is not longer specular but bulk diffusion reflection is governing the response due to scattering of light. At h=0, light already entered the slab and is detected by the detector fiber. However, this intensity is lower than the one found at h=1 since maximum is reached at higher heights as showed in Figure 6.7b.

2D

Scanning in x and y axis at $h = 2\ mm$ was performed to obtain 2D images (1.2x1.2 cm^2) of the surface of the materials being used. Optical fibers used were the regular POF already mentioned in Chapter 2 at wavelengths of 850 nm. Slabs of the meat were 3 mm thick with 40x4 μm^2 of resolution.

As we can see from Figure 6.9, surface roughness is significantly noticeable when the medium used is air. For the case of water, since $n_s > n_w$, roughness becomes less important allowing backward scattering to be displayed. This is, reflectivity at normal incidence is lower for the case of water as medium and only sharp details are maintained. The part of the slab displayed in 6.9 immersed in water, brighter zones could show a nerve present in the meat.

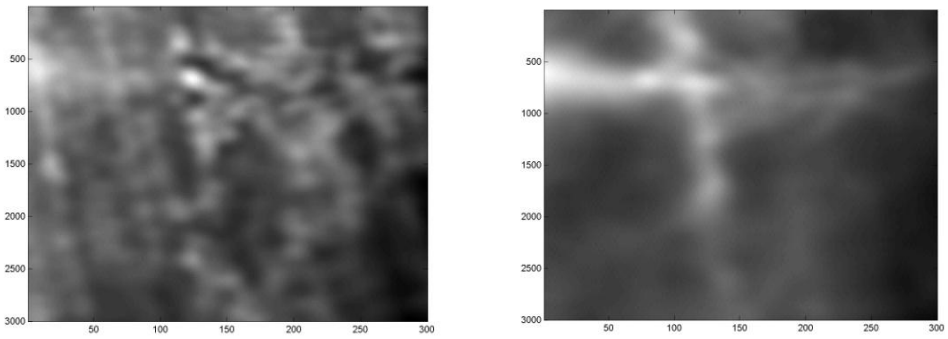

Figure 6.9 2D Surface study of a slab of cow muscle in air medium (left) and immersed in water medium (right).

In order to increase the 2D images resolution, finer optical fibers of 62.5 μm of diameter were used (so that cones of emission and reception of the fibers are narrower). Scanning resolution was enhanced from 40x4 μm^2 to 20x4 μm^2 for an image of 1.2x1.2 cm^2 as in the case of Figure 6.9. The material used as target was a human skin and is displayed in Figure 6.10. Shadows regarding the source of illumination are uniformly distributed all over the image since emitter fiber and detector fiber are moving together in the line of scanning, as a difference with optical microscopes where the source of light is fixed and shadows are not uniformly distributed.

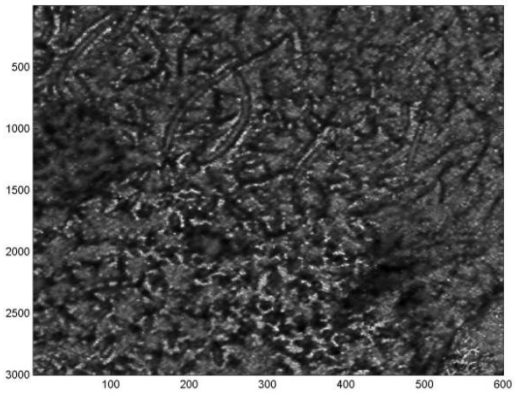

Figure 6.10 2D image of human skin: epidermis, stratum corneum (keratinocytes) in air as medium.

6.5 Discussion

Backward configuration is, undoubtedly, counter-intuitive. In order properly understand responses of the system a reliable numerical model should be developed which should take into account not only absorption phenomena but also scattering (one option is by using Monte Carlo method). The main data and experimental results have been already collected and described in this report.

If emitter optical fiber is fixed and receptor optical fiber is mobile in the horizontal axis, output intensity lowers as distance emitter-receptor increases. The slope of the distribution will vary as a function of the scattering being received by the receptor using properly prepared samples.

Possibility to change the configuration of the measuring system (from forward configuration to backward configuration) allows us to obtain 2D surface images to study bulk scattering (in water media much more noticeable). In order to enhance the study of this specific scattering, adaption of the refractive index between medium in contact with the target material and refractive index of the material should be done as explained in section 6.3.

Budget of the project

A detailed estimation of the costs of the project will be described. These costs are divided in two categories:

1. Personnel costs involved in the project.
2. Costs of Software, Hardware and fungible materials.

Costs are expressed in Euros. Software tools and equipment used are included in the final result.

Personnel Costs

In order to calculate the personnel costs, the people involved in the project as well as its role will be described. The cost per hour for each person is defined by an approximate value of the actual salary depending on their role. In Figure 7.1, the name of the participants, its category, the cost per hour, the total number of hours dedicated to the project and the final cost is shown. Jose Luis Muñíz was the supervisor and director of the project. Edilia Almeida and Mirentxu Santos were in charge of providing and teaching the student how to obtain tissue and blood samples.

Name	Category	Total hours	Euros/h	Final Cost
Jorge Ripoll	Professor	30h	35€	1050€
Jose Luis Muñíz	Researcher	60h	35€	2.100€
Cristina Herráez	Junior Engineer	280h	20€	5.600€
Edilia Almeida	Research Assistant	1h	30€	30€
Mirentxu Santos	Researcher	2h	35€	70€
Total Cost				**8.850€**

Figure 7.1 Detailed personnel costs.

Software, Hardware and Other Costs

The cost of the different materials and samples used (different media used along the experiments), computers to analyze the data (and licenses) are included in this subsection. In Figure 6.2 the product used, it costs, and the number of days that the product has been used is shown.

Product	Price	Use of the product	Final Cost for the project
Measuring system	100€/day	40 days	4000€
MATLAB license	6000€	-	3000€
Computer	600€	-	600€
Materials	20€	-	20€
Total Cost			**7.620**€

Figure 7.2 Detailed software, hardware and material costs.

Total Cost of the Project

Finally, the total sum of the costs of the different categories of the project is shown in Figure 7.3.

Description	Total Cost
Personnel Costs	8.850€
Software and Hardware Costs	7.600€
Materials Costs	20€
Total Cost	**16.470**€

Figure 7.3 Total cost of the project.

The total cost of the project is **16.470€.**

Conclusions and Future Work

The characterization of the measuring system provided by CIEMAT was successfully performed with an approximation accurately enough in different conditions for the analysis done along the study. Results adjust Gaussian functions of different index depending on the medium (air or water) used for the specific measurements.

Although the model for the characterization was approximated enough, demonstration of the need of a 2D implementation was evident when placed an obstacle between detector optical fiber and receptor optical fiber in highly scattering media, such as milk. For highly absorptive media, the model still adjusts accurately. However, the model does not adjust to reality for scattering media since extinction of light due to scattering is a complex process.

Having into account that most biological tissues approximates to highly scattering media, a deeper study of this phenomena in different conditions must be performed. The real responses of the system to highly scattering media in backward configuration become even more difficult to predict and are considered as counter-intuitive due to the results obtained. The numerical model that could reproduce these phenomena could be implemented following Monte Carlo method, although this implementation is out of the scope of the project.

The use of 2D images obtained out during the study in backward configuration evidence different facts depending on the medium used. If the system in this configuration is used in air, a study of the roughness of the sample being analyze is possible. If the system is used in water, a deep study of the bulk scattering can be performed.

The possibility offered to the student to change not only the configuration of the measuring system provided by CIEMAT but also the optical fibers of used, the wavelength of the source of light and the media during the experiments, allowed the student to acquire a wider knowledge not only in optical terms but also in the area of electronics and physics. Moreover, the student was trained on fibers preparation and had the opportunity to see the extraction of blood and biological tissue *in vivo* from mice by the corresponding trained personal. The limitation of time was not an impediment for the student to acquire new skills in the biomedical engineering field reaching and exceeding the aims set at the beginning of the description of the project.

Future work

Bearing in mind that this study is an introduction to the micro-illumination with optical fibers using this concrete measuring system, the future possibilities are wide not only regarding this system but the optical imaging technique in general. These possibilities range from the exploitation of the technology to 3D imaging to the deposition of energy on a localized area of different tissues. In a first step, improvements should be performed in the geometrical model so that it incorporates a fully spatial characterization of the expected illumination.

Secondly, in order to fulfill the requirement of 'minimum invasiveness', narrower fibers should be employed along the study. Fibers with diameters as small as 5 micrometers (Mode Field Diameter) for wavelengths in the important range of ultraviolet-blue are already commercially available. To handle such small (fully Gaussians) light spots in tissues implies a challenge that has not been yet completely solved.

Once these non-trivial questions are answered, we will be able to use this technology to open new possibilities in the development for the diagnostic of diseases such as cancer. Moreover, not only diagnostic but also healing these diseases will be possible by using the specific tools. In this context, a realistic characterization of the responses (optical, acoustical, electrical responses…) of different tissues to this extremely localized illumination would be very useful for designing this new generation of instruments. This means that optical imaging can be used as '*theranostics*' combining diagnosis and local therapy.

To accomplish this objective, both experimental and theoretical work should be done, developing a realistic model that can be tested with the help of the experimental (reconfigurable) facility used in this thesis. Introduction to the complex mathematical background knowledge needed for the suitable development of the technique can be also found in this document. Challenges regarding depth penetration and spatial resolution issues will be overcome allowing fusing optical imaging with other techniques (photoacoustic imaging or MRI) leading to more complete results by adding anatomical information.

ANNEX 1

Model that characterizes the receptor in air media.

MATLAB code:

```
clear inten
clear pos

resx=0.004;
w=0.50;
center=6450;
F=center*resx;


h0=27;

for i=1:16000
    h=h0-(i-center)*resx*tan(0.15);
    x=i*resx;
    pos(i)=x;
    alfa=atan((x-F)/h);
    inten(i)=(cos(alfa)^3/h^2)*exp(-
2*(abs(alfa)/w)^2.5)*cos(alfa)^0.5;
end
```

ANNEX 2

Model that characterizes the receptor in water media.

Matlab code:

```
clear inten
clear pos

resx=0.004;
w=0.38;
center=6450;
F=center*resx;


h0=27.81;

for i=1:16000
    h=h0-(i-center)*resx*tan(0.15);
    x=i*resx;
    pos(i)=x;
    alfa=atan((x-F)/h);
    arg=1.33*sin(alfa);
    inten(i)=(cos(alfa)^3/h^2)*exp(-
2*(abs(alfa)/w)^3)*cos(asin(arg))^0.5;
     if (arg>=1) || (arg<=-1)
        inten(i)=0;
    end
end
```

ANNEX 3

Model that characterizes the emitter in air media.

MATLAB code:

```
clear inten
clear pos

resx=0.004;
w=0.50;
centre=6450;
F=centre*resx;
rese=0.02;
resy=0.02;

h0=19.9;
inten(1:16000)=0;

for i=1:16000
    h=h0-(i-centre)*resx*sin(0.01);
    x=(i-8000)*resx;
      for j=1:21
          pos(j)=(j-11)*resy;
          for jl=1:21
              emi(jl)=(jl-11)*rese;
              beta=atan((x+pos(j)-emi(jl))/h);
              inten(i)=inten(i)+(cos(beta)^3/h^2)*exp(-
2*((abs(beta)/w)^2.5))*exp(-
2*((abs(beta)/w)^2.5))*(3*abs(cos(beta-
0.05)^700)+50*abs(cos(beta+0.75)^3.4));
          end
      end
end
```

ANNEX 4

Model that characterizes the emitter in water media.

```
clear inten
clear pos

resx=0.004;
w=0.33;
centre=6450;
F=centre*resx;
rese=0.02;
resy=0.02;

h0=3.9;
inten(1:16000)=0;

for i=1:16000
    h=h0-(i-centre)*resx*sin(0.01);
    x=(i-8000)*resx;
      for j=1:21
          pos(j)=(j-11)*resy;
          for jl=1:21
              emi(jl)=(jl-11)*rese;
              beta=atan((x+pos(j)-emi(jl))/h);
              inten(i)=inten(i)+(cos(beta)^3/h^2)*exp(-
2*((abs(beta)/w)^3))*exp(-2*((abs(beta)/w)^3))*(4*abs(cos(beta-
0.05)^700)+50*abs(cos(beta+0.1)^36));
          end
      end
end
```

ANNEX 5

Model that characterizes the emitter half covered in air media.

```
clear inten
clear pos

resx=0.004;
w=0.50;
centre=6450;
F=centre*resx;
rese=0.02;
resy=0.02;

h0=10.72;
inten(1:16000)=0;

for i=1:16000
    h=h0-(i-centre)*resx*tan(0.01);
    x=(i-8000)*resx;
      for j=1:21
          pos(j)=(j-11)*resy;
          efe=1;
          for jl=11:21
              emi(jl)=(jl-11)*rese;
              beta=atan((x+pos(j)-emi(jl))/h);
              inten(i)=inten(i)+(cos(beta)^3/h^2)*exp(-
2*((abs(beta)/w)^2.5))*exp(-
2*((abs(beta)/w)^2.5))*(13.5*abs(cos(beta-
0.05)^900)+50*abs(cos(beta+0.12)^44));
          end
      end
end
```

ANNEX 6

Model that characterizes the emitter by using the unwrapped fiber described in Configuration 1.

```
clear inten
clear pos

resx=0.004;
w=0.50;
centre=6450;
F=centre*resx;
rese=0.02;
resy=0.02;

h0=19.9;
inten(1:16000)=0;

for i=1:16000
    h=h0-(i-centre)*resx*sin(0.01);
    x=(i-8000)*resx;
      for j=1:11
          pos(j)=(j-6)*resy;
          for jl=1:11
              emi(jl)=(jl-6)*rese;
              beta=atan((x+pos(j)-emi(jl))/h);
              inten(i)=inten(i)+(cos(beta)^3/h^2)*exp(-
2*((abs(beta)/w)^2.5))*exp(-
2*((abs(beta)/w)^2.5))*(3*abs(cos(beta-
0.05)^1000)+60*abs(cos(beta+0.75)^3.6));
          end
      end
end
```

ANNEX 7

Model that characterizes the emitter by using the wrapped fiber described in Configuration 1.

```
clear inten
clear pos

resx=0.004;
w=0.50;
centre=6450;
F=centre*resx;
rese=0.02;
resy=0.02;

h0=19.9;
inten(1:16000)=0;

for i=1:16000
    h=h0-(i-centre)*resx*sin(0.01);
    x=(i-8000)*resx;
      for j=1:11
          pos(j)=(j-6)*resy;
          for jl=1:11
              emi(jl)=(jl-6)*rese;
              beta=atan((x+pos(j)-emi(jl))/h);
              inten(i)=inten(i)+(cos(beta)^3/h^2)*exp(-
2*((abs(beta)/w)^2.5))*exp(-
2*((abs(beta)/w)^2.5))*(3*abs(cos(beta-
0.05)^1000)+60*abs(cos(beta+0.75)^3.2));
          end
      end
end
```

ANNEX 8

Código de matlab para el ajuste en agua

```
clear inten
clear pos

resx=0.004;
w=0.33;
centre=6450;
F=centre*resx;
rese=0.02;
resy=0.02;

h0=12.5;
inten(1:16000)=0;
hf=5;

for i=1:16000
    x=(i-8000)*resx;
      for j=1:21
          pos=(j-11)*resy;
          for jl=1:21
              emi=(jl-11)*rese;
              beta=atan((x+pos-emi)/h0);
              l1=(h0*(0.5-emi))/hf + emi;
              l2=(h0*(1.3+emi))/hf - emi;
              factor=1;
                if ((x+pos)<=l1) && ((x+pos)>=-l2)
                  factor=0;
                end
             inten(i)=inten(i)+factor*(cos(beta)^3/h0^2)*exp(-
2*((abs(beta)/w)^3))*exp(-2*((abs(beta)/w)^3))*(4*abs(cos(beta-
0.05)^700)+50*abs(cos(beta+0.1)^36));
          end
      end
end
```

ANNEX 9

Código de matlab para el ajuste en agua con atenuación

```
clear inten
clear pos

resx=0.004;
w=0.33;
centre=6450;
F=centre*resx;
rese=0.02;
resy=0.02;
att=0.2;
h0=8.5;
inten(1:16000)=0;
hf=5;

for i=1:16000
    x=(i-8000)*resx;
      for j=1:21
          pos=(j-11)*resy;
          for jl=1:21
              emi=(jl-11)*rese;
              beta=atan((x+pos-emi)/h0);
              d=sqrt((x+pos-emi)^2+h0^2);
              l1=(h0*(0.66-emi))/hf + emi;
              l2=(h0*(1.14+emi))/hf - emi;
              factor=1;
                if ((x+pos)<=l1) && ((x+pos)>=-l2)
                  factor=0;
                end
             inten(i)=inten(i)+factor*(cos(beta)^3/h0^2)*exp(-
2*((abs(beta)/w)^3))*exp(-2*((abs(beta)/w)^3))*(4*abs(cos(beta-
0.05)^700)+50*abs(cos(beta+0.1)^36))*exp(-att*d);
          end
      end
end
```

References

[1] Q. Liu, “Role of optical spectroscopy using endogenous contrasts in clinical cancer diagnosis.,” *World J. Clin. Oncol.*, vol. 2, no. 1, pp. 50–63, Jan. 2011.

[2] S. C. Gebhart, W. C. Lin, and a Mahadevan-Jansen, “In vitro determination of normal and neoplastic human brain tissue optical properties using inverse adding-doubling.,” *Phys. Med. Biol.*, vol. 51, no. 8, pp. 2011–27, Apr. 2006.

[3] E. Pastrana, “Optogenetics: controlling cell function with light,” *Nat. Methods*, vol. 8, no. 1, pp. 24–25, Dec. 2010.

[4] C. G. Hadjipanayis, H. Jiang, D. W. Roberts, and L. Yang, “Current and future clinical applications for optical imaging of cancer: from intraoperative surgical guidance to cancer screening.,” *Semin. Oncol.*, vol. 38, no. 1, pp. 109–18, Feb. 2011.

[5] a P. Gibson, J. C. Hebden, and S. R. Arridge, “Recent advances in diffuse optical imaging,” *Phys. Med. Biol.*, vol. 50, no. 4, pp. R1–R43, Feb. 2005.

[6] F. Bevilacqua, D. Piguet, P. Marquet, G. Gross, B. Tromberg, and C. Depeursinge, “In vivo local determination of tissue optical properties: applications to human brain,” *Appl. Opt.*, vol. 38, no. 22, pp. 4939–4950, 1999.

[7] S. J. Erickson, S. L. Martinez, J. DeCerce, A. Romero, L. Caldera, and A. Godavarty, “Three-dimensional fluorescence tomography of human breast tissues in vivo using a hand-held optical imager.,” *Phys. Med. Biol.*, vol. 58, no. 5, pp. 1563–79, Mar. 2013.

[8] M. Herranz and a Ruibal, “Optical imaging in breast cancer diagnosis: The next evolution,” *J. Oncol.*, vol. 2012, no. 863747, p. 863747, Jan. 2012.

[9] L. C. L. Chin, W. M. Whelan, and I. A. Vitkin, *Optical-Thermal Response of Laser-Irradiated Tissue*. Dordrecht: Springer Netherlands, 2011.

[10] R. B. Schulz and W. Semmler, “Fundamentals of optical imaging,” *Handb. Exp. Pharmacol.*, vol. 185, no. PART1, pp. 3–22, 2008.

[11] U. Zacatenco, “Estudio de la Reflexión Óptica Difusa en Tejido Biológico,” pp. 1–90.

[12] “Light scattering a brief introduction. .” Available: http://igm.fys.ku.dk/~lho/personal/lho/LS_brief_intro.pdf.

[13] S. L. Jacques, “Optical properties of biological tissues: a review.,” *Phys. Med. Biol.*, vol. 58, no. 11, pp. R37–61, Jun. 2013.

[14] a E. Profio, “Light transport in tissue.,” *Appl. Opt.*, vol. 28, no. 12, pp. 2216–2222, 1989.

[15] Ł. Jankowski, “Modelling and simulation of light propagation in non-aged and aged step index polymer optical fibres /.”

[16] W. Merkmale and O. Code, “Silicon PIN Photodiode Lead (Pb) Free Product - RoHS Compliant BPX 65,” vol. 10, pp. 1–6, 2011.

[17] S. J. Wetzel, “Coupling light emitting diodes to multimode optical fibers Wetz I , t phen Ja ~ T C upling ight Emittin ids to Multim de ptical Fibers,” 1993.

[18] A. G. Hallam, “Mode Control in Multimode Optical Fibre and its Applications,” no. November, 2007.

[19] P. Fibers, “Fiber optics 9.1 9.2,” no. born 1933, pp. 325–362.

[20] J. S. Witkowski and A. Grobelny, “Ray tracing method in a 3D analysis of fiber-optic elements,” vol. XXXVIII, no. 2, 2008.

[21] H. Buiteveld, J. H. M. Hakvoort, and M. Donze, “Optical properties of pure water” in *Ocean Optics XII*, 1994, pp. 174–183.

[22] B. Merkmale, “Golden DRAGON ® Plus with Chip Level Conversion (CLC) Lead (Pb) Free Product - RoHS Compliant LUW W5AM Vorläufige Daten / Preliminary Data LUW W5AM,” no. Clc, 2008.

[23] T. Patra, “Numerical Aperture of A Plastic Optical Fiber,” vol. 2, no. 1, pp. 258–263.

[24] I. Moreno and R. I. Tzonchev, “near-field irradiance,” vol. 45, no. 10, pp. 2265–2272, 2006.

[25] “Publications | Lighting Research Center.” Available: http://www.lrc.rpi.edu/publicationdetails.asp?id=211.

[26] R. Kohl, D. Milovic, E. Zerrad, and A. Biswas, “Perturbation of super-Gaussian optical solitons in dispersion-managed fibers,” *Math. Comput. Model.*, vol. 49, no. 7–8, pp. 1700–1709, Apr. 2009.

[27] “Mean Square Error (MSE).” [Online]. Available: http://srmo.sagepub.com/view/encyclopedia-of-survey-research-methods/n290.xml. [Accessed: 24-Sep-2014].

[28] L. J. Saunders, R. A. Russell, and D. P. Crabb, “The coefficient of determination: what determines a useful R^2 statistic?,” *Invest. Ophthalmol. Vis. Sci.*, vol. 53, no. 11, pp. 6830–2, Oct. 2012.

[29] M. Hébert and R. D. Hersch, “Classical Print Reflection Models : A Radiometric Approach,” vol. 48, no. 4, pp. 363–374, 2004.

[30] Z. Shilie, Z. Xianmin, and C. Kangsheng, “Far Field Pattern and Differential Mode Attenuation of POF *,” pp. 1–4, 2003.

[31] Jeunhomme, *Single-Mode Fiber Optics: Prinicples and Applications, Second Edition,*. CRC Press, 1989, p. 312.

[32] B. J. Skutnik, W. Neuberger, and S. Spaniol, “<title>Optical fibers for improved light delivery in photodynamic therapy and diagnosis</title>,” in *Biomedical Optics 2004*, 2004, pp. 107–112.

[33] G. L. E. D. Lamps, “New 5mm Blue and Green LED Lamps,” pp. 1–12.

[34] W. Merkmale, S. Advices, and O. Code, “IR-Lumineszenzdiode (850 nm) mit hoher Ausgangsleistung High Power Infrared Emitter (850 nm) Lead (Pb) Free Product - RoHS Compliant SFH 4350 Vorläufige Daten / Preliminary Data SFH 4350,” vol. 40, pp. 1–7, 2006.

[35] P. O. F. for D. C. W. 72 Tables, *POF - Polymer Optical Fibers for Data Communication: With 72 Tables*. Springer Science & Business Media, 2002, p. 433.

[36] M. A. Losada, J. Mateo, I. Garcés, J. Zubía, and J. A. Casao, “Analysis of Strained Plastic Optical Fibers,” vol. 16, no. 6, pp. 1513–1515, 2004.

[37] “Optical Fiber Loss Testing.” Available: http://www.belden.com/resourcecenter/documents/upload/optical_fiber_loss_testing.pdf.

[38] J. N. Kutz, J. A. Cox, and D. Smith, “Mode mixing and power diffusion in multimode optical fibers,” *J. Light. Technol.*, vol. 16, no. 7, pp. 1195–1202, Jul. 1998.

[39] T. C. Chu and A. R. McCormick, “Measurements of Loss Due to Offset, End Separation, and Angular Misalignment in Graded Index Fibers Excited by an Incoherent Source,” *Bell Syst. Tech. J.*, vol. 57, no. 3, pp. 595–602, Mar. 1978.

[40] “Tapered optical fiber for coupling to diffused optical waveguides.” 10-Apr-2003.

[41] “Tapered fiber tips for fiber optic biosensors.” Available: http://nsrdec.natick.army.mil/LIBRARY/90-99/R95-76.pdf.

[42] R. Koyama, K. Nakajima, and T. Kurashima, “Physical Contact Connection of Single-Mode Fiber with Cleaved and Unpolished Endface,” in *National Fiber Optic Engineers Conference*, 2012, p. NTh1D.6.

[43] M. Tao, Y. Jin, N. Gu, and L. Huang, “A method to control the fabrication of etched optical fiber probes with nanometric tips,” *J. Opt.*, vol. 12, no. 1, p. 015503, Jan. 2010.

[44] H. K. Bal, Z. Brodzeli, N. M. Dragomir, S. F. Collins, and F. Sidiroglou, “Uniformly thinned optical fibers produced via HF etching with spectral and microscopic verification.,” *Appl. Opt.*, vol. 51, no. 13, pp. 2282–7, May 2012.

[45] R. Hennessy, S. L. Lim, M. K. Markey, and J. W. Tunnell, “Monte Carlo lookup table-based inverse model for extracting optical properties from tissue-simulating phantoms using diffuse reflectance spectroscopy.,” *J. Biomed. Opt.*, vol. 18, no. 3, p. 037003, Mar. 2013.

[46] M. H. Kalos, U. N. C. D. Division, and U. S. A. N. D. Laboratory, *Methods in Monte Carlo solution of the radiation transport equation*. U. S. Army Chemical Corps, Nuclear Defense Laboratory, Army Chemical Center, 1962, p. 44.

[47] "Construction of a Wide-Field Optical Sectioning Microscope," no. January, 2004.

[48] D. Faber, M. Aalders, E. Mik, B. Hooper, M. van Gemert, and T. van Leeuwen, "Oxygen Saturation-Dependent Absorption and Scattering of Blood," *Phys. Rev. Lett.*, vol. 93, no. 2, p. 028102, Jul. 2004.

[49] "Multiple Scattering: an Invitation." Available: http://inside.mines.edu/~pamartin/con-paps/waves95x.pdf.

[50] S. G. Narasimhan, M. Gupta, C. Donner, R. Ramamoorthi, S. K. Nayar, and H. W. Jensen, "Acquiring scattering properties of participating media by dilution," *ACM Trans. Graph.*, vol. 25, no. 3, p. 1003, Jul. 2006.

[51] R. Splinter and B. A. Hooper, *An Introduction to Biomedical Optics*. CRC Press, 2006, p. 632.

[52] "The effect of different types/brands of soft drinks on the decay on meats." Available: http://www.academia.edu/1787958/_The_effect_of_different_types_brands_of_soft_drinks_on_the_decay_on_meats._.

[53] U. A. Gamm, *Quantification of Tissue Scattering Properties by Use of Fiber Optic Spectroscopy*. .

[54] A. Yodh and B. Chance, "SPECTROSCOPY AND IMAGING," no. March, pp. 34–40, 1995.

[55] "Optical Absorption of Fat." Available: http://omlc.org/spectra/fat/. [Accessed: 24-Sep-2014].

[56] H. J. Swatland, "Optical Properties of Meat," no. 1962, pp. 1–7, 2005.

[57] G. Marquez, L. V Wang, S. P. Lin, J. a Schwartz, and S. L. Thomsen, "Anisotropy in the absorption and scattering spectra of chicken breast tissue.," *Appl. Opt.*, vol. 37, no. 4, pp. 798–804, Feb. 1998.

[58] M. Y. H. Z. Y. and H. A. S. W. Harun, *Fiber Optic Sensors*. InTech, 2012.

[59] L. Reflection, "Geometrical Optics and Fiber Optics," pp. 1–11.